Research highlights

- Reveals the neuro-regenerative potential of the small, transparent adult vertebrate *Danionella cerebrum*, a novel model for central nervous system (CNS) repair studies.
- Demonstrates CNS regeneration using two visual functional recovery assays and longitudinal *in vivo* imaging of a novel adult axonogenesis reporter transgenic line, a myelin reporter line, and mosaic labeling of retinal ganglion cell axons.
- Establishes a method to compare retinal ganglion cell axons before and after CNS injury in adult *D. cerebrum*.
- Positions *D. cerebrum* as a powerful platform for visualizing long-distance CNS regeneration in intact adult vertebrates.

Graphical abstract

Longitudinal live imaging of adult *D. cerebrum* reveals the formation of a new axon and myelin pattern post optic nerve injury along with functional recovery.

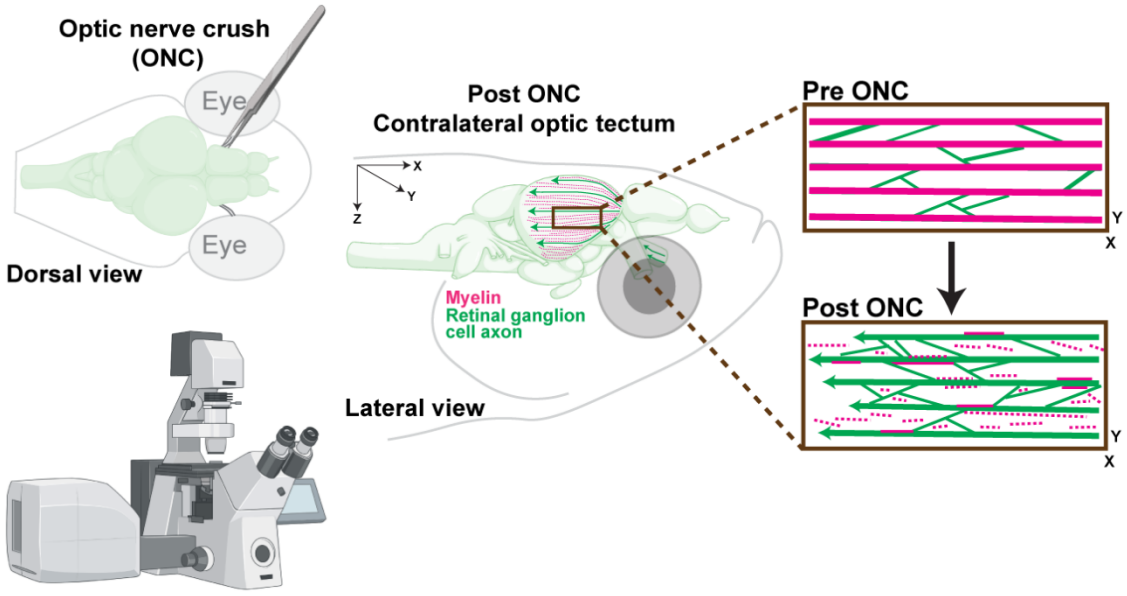

42 ***In vivo* imaging of central nervous system regeneration using *Danionella***
43 ***cerebrum***

44 Mallika Misyuk[1,2], Joseph L. Austin[1,2], Noelle R. Walechka[1,2], Juliet A. Peterka[1,2], Matthew B.
45 Veldman[2,3], Pui-Ying Lam[1,2,*]

46 [1]Neuroscience Research Center, Medical College of Wisconsin, Milwaukee, WI, USA
47 [2]Department of Cell Biology, Neurobiology and Anatomy, Medical College of Wisconsin,
48 Milwaukee, WI, USA
49 [3]Department of Ophthalmology and Visual Sciences, Medical College of Wisconsin,
50 Milwaukee, WI, USA

51 ***Corresponding author***
52 Pui-Ying Lam, PhD , plam@mcw.edu.
53 ORCID 0000-0002-6319-5752

54 ***Funding***
55 This work was supported by the National Institutes of Health Office of the Director under Award
56 Number R21OD033664 (to PYL), S10OD032136 (to Brandon Tefft - Medical College of
57 Wisconsin engineering core), and the Advancing a Healthier Wisconsin Endowment (to PYL).

58
59
60
61
62
63
64
65

Abstract

Rebuilding functional neuronal circuits after injury in the adult central nervous system (CNS) is unachievable for many vertebrates. In pro-regenerative models, it is unclear how regeneration and re-wiring is achieved in the CNS over long distances. The size and opacity of the adult vertebrate brain makes it difficult to study re-innervation patterns and dynamic cellular interactions during long-distance axon regeneration. Here, we harnessed the properties of the small and transparent adult *Danionella cerebrum* for longitudinal *in vivo* imaging of retinal ganglion cell axon regeneration, correlating cellular events with functional recovery. Our results suggest that, following optic nerve injury, the arborization pattern of re-innervation differs after regeneration, suggesting that new axon tracts are formed to restore functional vision. Additionally, myelin is not restored to pre-injury levels, even after functional recovery is achieved. The *D. cerebrum* model provides a unique opportunity to visualize and experimentally manipulate the spatial and temporal events during CNS regeneration in intact adult vertebrates.

Keywords: axon regeneration; central nervous system regeneration; *Danionella cerebrum*; functional recovery; in vivo imaging; myelin; neuroregeneration; optic nerve injury; retinal ganglion cell; transgenic model

92 ***Introduction***

93 It is well known that after a central nervous system (CNS) injury, most mammals fail to
94 sufficiently regenerate damaged axons to achieve proper target innervation. Long distance
95 axon regeneration after an optic nerve injury has been successfully induced in mice using
96 genetic manipulations (Park et al., 2008; Belin et al., 2015; Lim et al., 2016; Schaeffer et al.,
97 2023), however, functional recovery of vision fails since axons do not make proper
98 connections. Vision is restored after injury in pro-regenerative models, but it remains unclear
99 how the neuronal arborization patterning is re-established during regeneration, nor is it known
100 how axonal remodeling events during late regeneration contribute to functional recovery.

101

102 In nerve regeneration studies using vertebrate animals, the identification of key morphological
103 events traditionally requires histological sectioning of fixed tissue, and/or tissue clearing
104 (Chato-Astrain et al., 2022; Daeschler et al., 2022). Although optical tissue clearing techniques
105 have enabled three-dimensional imaging of entire organs, it has not been possible to image
106 dynamic cell-cell interactions, monitor the same animal over time, and correlate cellular events
107 with functional recovery. Alternatively, the use of intra-vital microscopy in the CNS of traditional
108 adult animal models requires the invasive implantation of an imaging window, yet allows for a
109 limited imaging field and depth (Suthya et al., 2024). To overcome this, larval zebrafish have
110 been used for the *in vivo* study of cellular dynamics and regeneration, owing to their small size
111 and transparency. However, larvae lack complex memory-based behaviors and fully
112 developed endocrine and neuro-immune systems, which makes it challenging to distinguish
113 between different phases of regeneration and functional recovery or to identify sex-based
114 differences and neuro-immune responses during regeneration (Murashova and Dyachuk,
115 2025). *Danionella cerebrum* (DC) is a new vertebrate model that provides a unique opportunity
116 to visualize the entire brain, *in vivo,* at single cell resolution. Adult DC remain largely optically
117 transparent, have the smallest known vertebrate brain, and lack a dorsal skull cap (Penalva-
118 Tena et al.; Penalva et al., 2018; Schulze et al., 2018a; Britz et al., 2021; Lam, 2022;
119 Lindemann et al., 2022; Rajan et al., 2022; Lee and Briggman, 2023; Cook et al., 2024;

120 Groneberg et al., 2024; Vasconcelos et al., 2024; Veith et al., 2024; Zada et al., 2024), which
121 makes DC particularly suitable for imaging cellular dynamics, especially in the CNS, in a live
122 animal without the need for surgical manipulations.
123
124 Investigating dynamic cellular biology during regeneration remains challenging in traditional
125 animal models due to limitations in size and transparency. The aim of this study was to
126 establish DC as a new model for longitudinal *in vivo* investigation of CNS regeneration and
127 functional recovery. We induced axonal injury in adult DC retinal ganglion cells (RGCs) by
128 adapting the optic nerve crush (ONC) technique, which has been used in other animal models
129 to study CNS regeneration (Bormann et al., 1998; Williams et al., 2020). To assess the
130 regenerative capacity of adult DC, we performed longitudinal live imaging using novel cell-
131 specific fluorescent reporter lines and correlated functional recovery with cellular events *in*
132 *vivo*. Our findings demonstrate that the DC model offers new opportunities for future studies
133 aimed at understanding how dynamic cellular events during regeneration contribute to
134 functional recovery.
135
136 ***Methods***
137
138 ***Fish husbandry and maintenance***
139 All animal work was carried out in accordance with the National Institutes of Health Guide for
140 Care and Use of Experimental Animals and approved by the Medical College of Wisconsin's
141 Institutional Animal Care and Use Committee protocol #AUA00007421 on 02/11/2023. All DC
142 (obtained from a cross between DC at the Bolton Museum Aquarium, Bolton, UK and wild-
143 caught samples purchased from The Wet Spot Tropical Fish store at Portland, OR, USA) were
144 maintained at 28°C on a 14-10 hour light-dark cycle. DC larvae were co-cultured with
145 euryhaline rotifers (*Brachonius plicatilis*) between 5 and 11 days post-fertilization (dpf).
146 Thereafter, they were placed into a re-circulating water system and fed rotifers once a day and
147 *Artemia nauplii* thrice a day until 14 dpf. Fish ≥ 1-month post-fertilization (mpf) were considered

148 adults and were fed with freshly hatched *Artemia nauplii* twice a day. Spawning was
149 encouraged by placing a ~6 cm white opaque silicone tube (6 mm inner diameter × 8 mm outer
150 diameter, McMaster-Carr, Elmhurst, IL, USA, Cat# 5054K812) on the bottom of tanks. After
151 collection of embryos, the media in the plate was exchanged every 24 h with E3 containing 10
152 mM HEPES (Gold Biotechnology, Olivette, MO, USA, Cat# H-400-250).
153
154 ***Generation of expression plasmids and transgenic lines***
155 Tol2-*gap43:mGreenLantern-CAAX* was made by performing a Multisite Gateway LR reaction
156 to assemble the following elements using LR Clonase II Plus enzyme (ThermoFisher
157 Scientific, Waltham, MA, USA, Cat# 12538120): *p5E-gap43, pME-mGreenLantern*, *p3E-*
158 *CAAX(tH)* (Addgene, Watertown, MA, USA, Cat# 109539) (Hall et al., 2020), and
159 *pDestTol2pA2* (Kwan et al., 2007). *p5E-gap43* was created by amplifying the *gap43* promoter
160 from plasmid *pW1GFG43SA* (Udvadia, 2008) using a polymerase chain reaction (PCR) with
161 the following primers: Forward (F): ggggacaactttgtatagaaaagttggtcgactgtgtggcttccg, and
162 Reverse (R): ggggactgctttttgtacaaacttgggttcaagttggttctatcctccct. The resulting PCR fragment
163 containing 3624 base pairs of the promoter, the transcription start site, and the 5'UTR
164 sequence stopping immediately before the initial ATG codon was integrated into the
165 pDONR^{TM}P4-P1R vector using a Gateway BP reaction. *pME-mGreenLantern-CAAX* was
166 created by amplifying *mGreenLantern* using *LifeAct-mGreenLantern* (Addgene Cat# 164459)
167 (Campbell et al., 2020) as a template and primers F:
168 ggggacaagtttgtacaaaaaagcaggctccaccatggtgagcaagggcgaggagctg,
169 and R: ggggaccactttgtacaagaaagctgggtgcttgtacagctcgtccatgtcatg. The PCR product was then
170 cloned into *pDONR221* using a Gateway BP reaction. The *Tol2-mbpa:TdTomato-CAAX* and
171 *Tol2-isl2b:Tdtomato-CAAX* expression constructs were created using Gateway LR reactions
172 and combining either *p5E-mbpa* or *p5E-isl2b* (Ben Fredj et al., 2010) with *pME-TdTomato-*
173 *CAAX* (Addgene, Cat# 135204) (Oehlers et al., 2015), *p3E-polyA* (Tol2kit # 302) (Kwan et al.,
174 2007) and *pDestTol2pA2* (Kwan et al., 2007). The zebrafish *mbpa* promoter (Jung et al., 2010;
175 Pinzon-Olejua et al., 2017) was amplified from genomic DNA using primers F:

176 ggggacaactttgtatagaaaagttggcttacactcactgacaaatag and R:
177 ggggactgctttttgtacaaacttgtctaggtgttgatctgttcag, then integrated into the *pDONR^{TM}P4-P1R*
178 vector using a Gateway BP reaction to create *p5E-mbpa*.
179
180 All single transgenic lines and sparsely labeled fish were generated by microinjection of 2-3
181 nL of a DNA-transposase mixture into 1-4 cell stage *wild-type* (*WT*) DC embryos. The DNA-
182 transposase mixture contained 8-8.8 ng/µL of DNA, 12.6 ng/µL *in vitro* transcribed Tol2
183 transposase mRNA (mMESSAGE mMACHINE™ SP6 Transcription Kit, ThermoFisher
184 Scientific, Cat# AM1340) and 0.05% phenol red (Sigma Aldrich, Burlington, MA, USA, Cat#
185 P0290) as an indicator. Injected larvae were screened at 4 dpf and animals positive for reporter
186 expression were raised to adults. To generate stable transgenic lines, adult F0 fish were in-
187 crossed to produce F1 embryos that were screened for correct and complete transgene
188 expression. Double transgenic lines were generated by outcrossing fish of the opposite sex
189 from each transgenic line.
190
191 ***Generation of microphthalmia-associated transcription factor (mitf) mutant line***
192 Target sites for CRISPR/Cas9-directed mutagenesis were selected with the help of the online
193 tool CHOPCHOP (Montague et al., 2014; Labun et al., 2016; Labun et al., 2019). A *mitf* gRNA
194 (5'- GGGAGCCAAACTCAGCCCTC -3') targeting exon 5 of the DC *mitf* gene was used to
195 generate the *mitf* knockout. The generation of the sgRNA template and its subsequent
196 transcription followed previously published protocols (Parvez *et al.,* 2021). Briefly, the DNA
197 template for *in vitro* transcription was generated using a fill-in reaction of two annealed oligos.
198 One oligo contained the *mitf* targeting sequence along with the SP6 promoter sequence
199 (underlined)
200 <u>ATTTAGGTGACACTATAG</u>GGAGCCAAACTCAGCCCTCGTTTTAGAGCTAGAAAT
201 AGCAAG. The second oligo contained the constant region
202 AAAAGCACCGACTCGGTGCCACTTTTTCAAGTTGATAACGGACTAGCCTTATTTTAACTT
203 GCTATTTCTAGCTCTAAAAC. The fill-in reaction used the following parameters: 98°C - 2

204 min, 50°C - 10 min, 72°C - 10 min, 4°C - Hold. The annealed and filled-in oligo was purified
205 using a Zymo DNA Clean and Concentrator-5 kit (Zymo Research, Irvine, CA, USA, Cat#
206 D4013). *In vitro* transcription was performed using MEGAscript™ SP6 Transcription kit
207 (ThermoFisher Scientific, Cat# AM1330) according to manufacturer's guidelines. Samples
208 were then purified using an RNA Clean and Concentrator-5 (Zymo Research, Cat# R1013). A
209 5 µL injection mixture was prepared with Buffer 3.1, 1000 ng gRNA, 0.84 µL EnGen Cas9
210 (NEB, Ipswich, MA, USA, Cat# M0646T). Then, 0.5 nL of the injection mixture was injected
211 into 1-2 cell stage embryos. Genotyping of crispants, *WT* controls, and putative *mitf*$^{-/-}$ F1
212 animals was carried out by first extracting genomic DNA from tail fin clips (for adults) or from
213 cells isolated by using a Zebrafish Embryo Genotyper (Lambert et al., 2018) (for larvae). PCR
214 primers CCCACATGCCTAAACTTTGCAC and GTTGAGGGTGAGAAGGGCCA flanking the
215 gRNA targeted site were used for PCR amplification of genomic DNA using Phire tissue direct
216 PCR master mix (ThermoFisher Scientific, Cat# F170S). PCR products were then purified and
217 sequenced.
218
219 ***ONC and Optic Nerve Transection (ONT)***
220 Adult DC were anaesthetized using 52.24 µg/mL Tricaine-S (ThermoFisher Scientific, Cat#
221 NC0342409) diluted in fish system water. The fish was positioned on a custom 3-D printed
222 (Lam 2022) holder at an oblique angle with the eye to be injured facing up. Excess fish water
223 was removed. Under a dissecting microscope with bottom illumination, the optic nerve was
224 exposed by gently removing the connective tissue on the dorsal half of the eye and rotating
225 the eye out of its socket. Using a #5 forceps (Electron Microscopy Sciences, Hatfield, PA,
226 USA, Cat# 0203-5-PS-1), ONC was carried out by closing the forceps on the optic nerve gently
227 for 5 s while avoiding the ophthalmic artery posterior to the optic nerve. Similarly, ONT was
228 carried out by cutting the optic nerve using micro-scissors (Fine Science Tools, Foster City,
229 CA, USA, Cat# 15000-08). Immediately after the procedure, the ONC/ONT site was assessed
230 under a dissecting microscope. A successful ONC was determined if the crushed site became
231 opaque and the axonal tissue remained attached. A successful ONT was determined if the

232 optic nerve head was fully detached from the rest of the optic nerve. The fish were then placed
233 in a recovery tank for approximately 15 minutes or until the fish resumed normal swimming,
234 after which they were transferred to the circulating tank system in the fish facility.
235
236 ***Looming Response (LR) assay***
237 To analyze the recovery of vision in adult DC post optic nerve injury, we adapted an LR assay,
238 that was previously established in zebrafish to assess looming visual stimulus-evoked escape
239 responses (Temizer et al., 2015; McKee and McHenry, 2020). The LR assay was performed
240 in a custom-made blackout box measuring 45 cm × 38 cm × 30 cm. The box had a hinged
241 front door and was lit with a uniform white LED light source (NXENTC A4 Tracing Light Pad,
242 Amazon, Seattle, WA, USA, ASIN: B07D57F8X7) set to maximum brightness (1630 lx) to
243 provide contrast for recording and tracking of fish. The fish was placed in a clear plastic tank
244 (Michaels, Irving, TX, USA, Cat# 10728059) measuring 10.16 cm × 20.32 cm × 7.62 cm and
245 filled with 770 mL of fish water maintained at 24 - 28°C. The bottom and lateral insides of the
246 tank were covered in matte-clear tape (Gaffer Power Transparent Duct Tape, Amazon, ASIN:
247 B076J2BS1B) to reduce internal reflection. The tank was placed in the blackout box 2.9 cm
248 away from the LED light screen. The camera (Logitech, Lausanne, Switzerland, P/N: 860-
249 000451, 1080p, 30fps) was placed 33 cm from the light screen to capture images of the whole
250 tank. A Raspberry Pi monitor, 15×23.5 cm (ROADOM Raspberry Pi Screen, Amazon, ASIN:
251 B09XDK2FRR), mirrored a computer monitor that played the stimulus video. The monitor was
252 centered and placed face down at 2.54 cm above the water. The stimulus video was created
253 using Adobe Premiere Pro 2024 (Adobe, San Jose, CA, USA, Version 24.0.1). The video
254 projected a white screen for 2 min, followed by a looming stimulus presented as an expanding
255 circle. The opacity, expansion speed and final size of the circle were optimized to illicit a robust
256 change in swimming speed of uninjured *WT* fish while the stimulus appeared. An expanding
257 opaque black circle that grew from 0 to 10.8 cm at a radius growth rate of 5.4 cm/s was used.
258 The opaque black circle expanded over 2 s and remained on the screen for one minute. As
259 the stimulus appeared, a grey rectangle appeared on the right side of the screen to allow for

accurate tracking of the stimulus during analysis. This grey rectangle was reflected to the camera by a mirror (Iconikal Metal Compact, Amazon, ASIN: B0B75R1K8N) placed beside the tank.

Fish can respond to a looming stimulus even with one functional eye. To accurately assess the time-course of vision recovery post ONC, an ONT was first performed on the left eye of the fish to induce permanent blindness in that eye, followed by an ONC on the right eye of the same fish one day later. A LR assay was performed on the same fish over the course of 12 days to assess the recovery of vision on the ONC-injured eye. The fish was given adequate time (5-20 min) to acclimate to the looming tank environment before the looming assay was performed. Acclimation was considered complete when the fish displayed leisurely swimming throughout tank.

An ANY-Maze video tracking system (ANY-Maze, Dublin, Ireland, Version 7.4) was used for animal tracking. A Python code was created to analyze the data generated from ANY-Maze. The code identified the exact time the visual stimulus appeared by detecting the change in pixel intensity in the reflection of the mirror. The code averaged the swim speed of the fish 1 s before the stimulus and 1 second as the stimulus was played. 2-3 trials were conducted per fish for each time-point. Fish showed minimal looming responses at 1-day post ONC (dpONC). The average change in speed at this time-point was used as the baseline for determining a reaction score. If a trial's average change in speed was greater than one standard deviation of the average change in speed at 1 dpONC, the trial scored a 1 and considered a positive response, otherwise, the trial scored a 0 and was considered a non-response. The score was averaged for the trials at each time-point for each fish. The scores were converted to a percentage and graphed using GraphPad Prism (GraphPad Software, San Diego, CA, USA, Version 10.4.1).

Dorsal light response (DLR) assay

288 The DLR assay (Watanabe et al., 1989; Lindsey and Powers, 2007; Mensinger and Powers,
289 2007; Beckers et al., 2023) was adapted for DC and used to investigate the behavioral
290 response of fish to visual stimuli by quantifying the tilt angle of the head orientation while
291 swimming. Single fish were acclimated for 5 to 10 minutes (until normal swim behavior was
292 observed) in a clear acrylic chamber (6 cm× 6 cm× 6 cm) containing 130 mL of fish water
293 maintained at 24-26°C. Each apparatus had two side-by-side chambers, allowing for
294 simultaneous recording of two fish. The lateral and bottom insides of the chamber were lined
295 with 100% light blocking white vinyl (VELIMAX White Blackout Window Film, Amazon, ASIN:
296 B08P8KQCL4), while the front was covered with one-way mirror film (KESPEN Window
297 Privacy Film One Way, Amazon, ASIN: B07PBTWCXC) with 28% visible light transmission,
298 oriented such that the reflective side faced inward. The back side of the chamber remained
299 transparent. A uniform white LED light source (Invitrogen, Carlsbad, CA, USA, Cat# LB0100)
300 illuminated the chamber from the back, operating at its maximum light intensity (17900 lx)
301 setting to provide optimal contrast for video capture.
302
303 Fish were filmed swimming toward the mirror film using a camera (iPhone 11, 1080p
304 resolution, 30 fps) positioned 12.5 cm away from the front of the chamber. The camera was
305 focused on the center of the chamber, with fish monitored during recording to ensure head-on
306 views were captured. Video recordings varied in length from less than 1 minute to
307 approximately 5 minutes. For analysis, 3-5 frames were captured from each video recording,
308 where the fish was positioned head-on relative to the camera. Head tilt angles were measured
309 from the captured frames using Fiji (ImageJ Version 1.54p, NIH, Bethesda, MD, USA)
310 (Schindelin et al., 2012). Specifically, the straight-line tool was used to draw a line connecting
311 the top pixel of one eye to the top pixel of the other eye. This line was aligned at the intersection
312 of a cross to facilitate the angle measurement. The angle was quantified using the angle tool
313 in Fiji. The change in head tilt angle was normalized by subtracting the head tilt angle at pre
314 ONC time-point to each time-point. Fish possessing a change in head tilt angle above 10

315 degrees at 1 dpONC were considered for further analysis. The change in head tilt angle was
316 measured over several days and plotted using GraphPad Prism.
317
318 ***Fish mounting and intubation for imaging***
319 *For larval DC*: At the desired developmental stage, larval DC were anaesthetized using 200
320 µg/mL Tricaine-S diluted in E3 containing 10 mM HEPES. Anaesthetized larvae were mounted
321 for imaging using 1% low melt agarose (Apex Bioresearch, Houston, TX, USA, Cat# 20-104)
322 in E3 in the desired orientation on a 3.5 cm glass bottom petri dish (Cellvis, Mountain View ,
323 CA, USA, Cat# D35-20-0-N). Once the agarose had hardened, 2 mL of 200 µg/mL Tricaine-S
324 in E3 was added to the petri dish to cover the agarose.
325
326 *For adult DC*: Fish were lightly anaesthetized with 65 µg/mL Tricaine-S diluted in fish water
327 and then embedded in 4% low melt agarose dissolved in E3 buffered with 10mM HEPES on
328 a custom imaging chamber equipped with an intubation inflow tube that was placed inside the
329 mouth of the fish, supplying fresh fish water for the duration of imaging, as previously
330 described (Lam, 2022). For long-term time-lapse imaging of regeneration, fish were mounted
331 and then intubated with 65 µg/mL Tricaine-S diluted in fish water for the duration of imaging.
332
333 ***Image acquisition***
334 All images were acquired using the NIS elements software (Nikon, Minato City, Tokyo, Japan,
335 Version 5.41.01) on a Nikon Ti2 inverted microscope (Nikon) fitted with a Yokogawa CSU-W1
336 spinning disk confocal head (Yokogawa Co., Hachioji City, Tokyo, Japan). Images were
337 captured using a Prime 95B Scientific CMOS camera (Teledyne Vision Solutions, Waterloo,
338 Ontario, Canada), and fluorophores were excited using a 488 nm or 561 nm excitation laser.
339 Images were captured using the following objectives: 4× Air 0.2 Numerical aperture (N.A.), 10
340 × Air 0.45 N.A., 20× Air 0.75 N.A. or 40× Water 1.25 N.A.
341

342

343 ***Analysis of gap43 reporter signal***

344 All quantification was performed using Fiji (Schindelin et al., 2012) and graphs were generated
345 using GraphPad Prism. For the analysis of developmental downregulation of *gap43* reporter
346 signal in **Figure S4**, *gap43* reporter signal was quantified using maximum intensity projection
347 (MIP) images from confocal z-stack images. A fixed region of interest (ROI) was defined in the
348 hindbrain (HB), midbrain (MB), and forebrain (FB) using the bright-field image as guidance.
349 Mean signal intensity in the ROI was calculated and normalized to 2 mpf using the formula:
350 mean intensity in the ROI at X mpf time-point /2 mpf time-point. For the analysis of *gap43*
351 reporter signal in response to an optic nerve injury in **Figure 3K, 3Q** and **Figure S5K, S5L**,
352 *gap43* reporter signal was quantified using single z-plane images at the medial contralateral
353 optic tectum (cTeO; ROI as shown by the white dotted line in **Figure 3B'-G', B''-G''** and yellow
354 dotted line in **O-P**). The mean intensity under the line-ROI indicated in **Figure 3J** was
355 calculated at different time-points and normalized with pre ONC using the formula: mean
356 intensity the under the line-ROI at X dpONC time-point/ pre ONC. For the analysis of *gap43*
357 reporter signal in a z-plane where re-innervation was observed in the medial optic tectum
358 (TeO) in **Figure 3L**, the intensity of *gap43* reporter signal under the line-ROI from the rostral
359 to caudal cTeO was plotted.

360

361 ***Analysis of oligodendrocyte membrane reporter signal***

362 Quantification of oligodendrocyte membrane reporter signal was performed using Fiji
363 (Schindelin et al., 2012) and graphs were generated using GraphPad Prism. The pattern of
364 the oligodendrocyte membrane reporter signal shown in **Figure 6G** was analyzed by plotting
365 the mean signal intensity under a line ROI in the MIP image of the dorsal cTeO. Quantification
366 of the percentage area covered by the myelin signal in **Figure 6H** was performed in a defined
367 ROI in the rostral-dorsal TeO using MIP images. The ROI was selected to ensure that no
368 pigment spots were included in the quantification. The same signal thresholding parameters

369 were applied for each animal to quantify the percentage of area covered by the
370 oligodendrocyte membrane reporter *mbpa:TdTomato-CAAX*.
371
372 ***Analysis of distribution of sparsely labeled RGCs pre- and post-injury by depth***
373 Confocal z-stack images of sparsely labelled RGCs at pre- and post-ONC time points were
374 quantified for signal intensity by depth using Fiji (Schindelin et al., 2012) and graphs were
375 generated using GraphPad Prism. The post ONC image was registered to the pre ONC image
376 using the "BigWarp" Fiji plug-in (Schindelin et al., 2012) (Thuma et al., 2023). A fixed ROI in
377 the cTeO was used to plot the signal intensity by depth using the "plot z-axis profile" option in
378 Fiji (Schindelin et al., 2012).
379
380 ***Post-acquisition image processing and video rendering***
381 Post-acquisition, images in **Figure 3H-I,** and **Figs. 4-6** were subjected to Denoise.ai (NIS
382 elements, Version 5.41.01). For image registration across different time-points, an image from
383 the brightfield channel was used as a reference. Images in **Figs. 3-6** were registered in the X-
384 Y direction using the "Align Image by Line ROI" Fiji plug-in. Additionally, in **Figure 4B-E, 4B'-**
385 **E'** and **5E-N**, the "BigWarp" Fiji plug-in was also used for image alignment. In **Supplemental**
386 **Video 4**, video alignment was done using the FiJi plug-in "Linear Stack Alignment with
387 SIFT"(Lowe, 2004). In **Supplemental Video 5** and **6**, Denoise.ai and 3-D deconvolution (NIS
388 elements; parameters used were: "Deconvolution Method": Automatic, "Modality": Spinning
389 Disk, "Pinhole Size": 50.00 µm, "Magnification": 40.0x, "Numerical Aperture": 1.15, "Immersion
390 Ref. Index": 1.333, "Calibration": 0.275 µm/px, "Z-step": 0.400 µm) were applied. 3-D rendering
391 videos were created using the "Movie Maker" function in NIS elements. Adobe Premiere Pro
392 was used to add titles, annotations, timestamps, and to sync videos.
393
394 ***Statistical analysis***
395 Preliminary n number estimations were done using G*power (Kang, 2021) (Version 3.1.9.4; α
396 = 0.05, and power (1-β) = 0.95). All statistical analysis post data acquisition was performed

397 using GraphPad Prism. All data were tested for normal distribution using the Shapiro-Wilk
398 normality test. 1-way Analysis of Variance (ANOVA) was carried out when comparing means
399 of three or more independent groups. A Repeated Measures 1-way ANOVA was carried out
400 when comparing means of three or more groups that are dependent. A Repeated Measures
401 2-way ANOVA was carried out when means of two or more independent groups were
402 compared over time. The mixed effects ANOVA model was fitted when the sample size of each
403 group was different.
404
405 ***Results***
406 ***Adult D. cerebrum can functionally recover from an optic nerve injury***
407 In non-mammalian vertebrates, RGC axons exit the eye as the optic nerve and innervate the
408 TeO, the largest brain center for visual processing. After an optic nerve injury in zebrafish,
409 approximately 75% of RGCs survive (Zou et al., 2013) with axonal regeneration (Udvadia,
410 2008; Diekmann et al., 2015) leading to functional recovery (Mensinger and Powers, 2007;
411 Beckers et al., 2023; Hu and Veldman, 2025). It is not known if the CNS of adult DC can
412 regenerate. We established the ONC technique in adult DC to inflict a CNS injury (**Figure 1A-**
413 **A'**), then assessed their ability to regain vision using two behavioral assays, a DLR and a LR
414 assay. The DLR assay has been used to assess vision in fish. When vision is lost in one eye,
415 fish tend to tilt their body such that the eye that has lost vision faces upwards. The recovery
416 of head tilt correlates with the recovery of vision (Watanabe et al., 1989; Lindsey and Powers,
417 2007; Mensinger and Powers, 2007; Beckers et al., 2023; Hu and Veldman, 2025). Based on
418 this principle, we devised a DLR assay for adult DC to accommodate their small size and
419 transparency for video recording and analysis (**Figure 1B, S1A and Methods**). After
420 subjecting *WT* animals to an ONC, we measured the head tilt angle over the course of 18 days
421 (**Figure 1B' and 1C**). Compared to pre ONC, a significant change in head tilt angle was
422 observed at 1 dpONC (**Figure 1D;** Total pre ONC vs 1 dpONC *P value* < 0.0001). Head tilt
423 angle recovered by 18 dpONC, suggesting that adult DC can recover vision after an ONC
424 (**Figure 1D and Supplemental Video 1**). When we compared the recovery of males to

425 females, no significant difference was observed except at 10 dpONC (males vs females at 10
426 dpONC $P = 0.0449$).
427
428 To evaluate the functional vision of injured DC, we established an LR assay (**Figure 1E and**
429 **F and S1B**). This assay tests the ability of fish to detect a predatory stimulus and has been
430 used to assess visual function (Temizer et al., 2015; Dunn et al., 2016). Fish can display an
431 escape behavior in response to a looming stimulus with only one eye. To specifically assess
432 vision recovery from the ONC-injured eye, the optic nerve of one eye was first transected, then
433 an ONC was performed on the other eye one day later (**Figure 1G**). We used the DLR assay
434 to validate that vision did not recover after a full ONT in adult DC (**Figure S2;** Total pre ONT
435 vs 18 dpONC *P value* < 0.0001). The percentage of fish responding to a looming stimulus at
436 1 dpONC was significantly lower compared to those that responded pre-injury (**Figure 1H;** -1
437 dpONC vs 1 dpONC *P value* < 0.0001). However, 22.62% of the fish were scored as
438 responding to the stimulus at 1 dpONC despite having no intact optic nerves. This was likely
439 due to sporadic movement of the fish coinciding with stimulus. Vision recovery was observed
440 at 8 dpONC, although the percentage of fish that responded was still lower than at pre ONC
441 levels (**Figure 1H and Supplemental Video 2**). The time to recover from ONC, as determined
442 using the DLR assay differed from the LR assay. This might be due to the different synaptic
443 connections required to elicit different visual responses as it was shown that teleost fish use
444 different visual pathways when responding to different visual cues (Nevin et al., 2010).
445 Nonetheless, our results show that adult DC can recover from an ONC injury, the progress of
446 which can be assessed using a DLR and/or LR assay.
447
448 ***An axonogenesis reporter line for adult fish***
449 To facilitate the *in vivo* visualization of regenerating axons, we generated a novel transgenic
450 DC line, *Tg(gap43:mGreenLantern-CAAX)*. Previous work has shown that the *gap43* promoter
451 from Japanese pufferfish, *Takifugu,* can be used to track neuronal development and
452 regeneration in zebrafish (Udvadia, 2008). At early developmental stages (2 dpf), robust

453 *gap43* promoter-driven expression in the brain and eye was observed (**Figure 2A-D, 2A'-D'**
454 **and S3**) and persisted into the young adult stage (2.5 mpf) (**Figure 2E-E'**). *gap43* promoter-
455 driven expression was detected in different regions of the FB, MB, and HB at all depths
456 imaged, from the dorsal plane through to the ventral plane (**Figure 2G-I, 2G'-I', Supplemental**
457 **Video 3**). These observations demonstrated that this *gap43* promoter-based transgenic line
458 shows expression throughout the brain and allows for monitoring of neurogenesis in the entire
459 brain of adult DC.
460
461 The expression of the endogenous *gap43* gene is downregulated as the animal ages due to
462 the conclusion of neurogenesis (Reinhard et al., 1994; Karimi-Abdolrezaee et al., 2002). We
463 performed longitudinal imaging experiments on the same *Tg(gap43:mGreenLantern-CAAX)*
464 animals to quantify levels of *gap43* promoter-driven expression in multiple brain regions
465 (**Figure S4A**). We observed significant downregulation of *gap43* reporter signal in all 3 regions
466 of the brain at 6.5 mpf as compared to 2 mpf (for HB 2 mpf vs 6.5 mpf P value < 0.0001, for
467 MB 2 mpf vs 6.5 mpf P value = 0.0012, for FB 2 mpf vs 6.5 mpf P value = 0.0007). Although
468 levels had decreased in all regions tested, we could still detect signal at 6.5 mpf (**Figure S4B-**
469 **J**), suggesting that fish at this age continue to exhibit some degree of neurogenesis.
470
471 ***Axon regeneration in vivo***
472 To visualize RGC axon regeneration *in vivo*, we performed an ONC in adult
473 *Tg(gap43:mGreenLantern-CAAX)* fish then carried out longitudinal imaging on the same fish.
474 We observed an upregulation of *gap43* reporter signal in the cTeO starting at 4 dpONC,
475 followed by its downregulation by 9 dpONC (**Figure S5A-G**). Interestingly, when animals were
476 subjected to an ONT, there was no significant difference in the *gap43* reporter signal intensity
477 between pre ONT and 5 dpONT in the cTeO (**Figure S5H-K**). This suggests that a more severe
478 transection injury does not lead to the appearance of regenerating neurites and corroborates
479 our observation that animals receiving an ONT lack vision recovery when assessed using the

480 DLR assay (**Figure S2**). We originally generated the *Tg(gap43:mGreenLantern-CAAX)*
481 transgenic line in *WT* DC. The presence of melanophore pigment cells in the epidermal layer
482 dorsal to the brain (**Figure S5D**), dynamically changed their shape and hindered our ability to
483 quantify and compare the intensity of the *gap43* reporter signal in the same animal's brain
484 over time. To overcome this, we generated a DC pigmentation mutant for *in vivo* imaging of
485 neuro-regeneration. Mutating the *mitfa* gene in zebrafish produced fish that lack
486 melanophores (Lister et al., 1999). We identified the DC *mitf* gene using the NCBI DC Genome
487 assembly ASM722483v1, then designed gRNAs to generate a *mitf*$^{-/-}$ mutant line using
488 CRISPR-Cas9 mediated mutagenesis (**Figure S6A**). *mitf*$^{-/-}$ mutant DC have reduced
489 melanophore pigment cells when compared to *WT* fish, both at larval (**Figure S6B and C)** and
490 adult stages (**Figure S6D-I**). There was no significant difference in the looming response
491 between *mitf*$^{-/-}$ and *WT* animals, suggesting that *mitf*$^{-/-}$ fish have normal vision (**Figure S6J**).
492 We performed an ONC on *mitf*$^{-/-}$ animals and used the DLR assay to assess their ability to
493 regenerate. Results between *WT* and *mitf*$^{-/-}$ animals were similar (**Figure S6K**). One difference
494 we did observe, however, was that *mitf*$^{-/-}$ animals displayed a significantly slower swim speed
495 in response to a looming stimulus when compared to *WT* animals (**Figure S6L**; post stimulus
496 *WT* vs *mitf*$^{-/-}$*, P* value = 0.0001).
497
498 Pigment-deficient *mitf*$^{-/-}$ fish were used to generate a *Tg(gap43:mGreenLantern-CAAX)*
499 transgenic line. These fish were subjected to ONC and imaged over the course of 10 days.
500 The lack of pigment in this transgenic line allowed us to observe *gap43* reporter signal without
501 melanophore cell obstruction (**Figure 3A-I**). Growth cones of RGC axons were observed in
502 the cTeO at 4 dpONC (**Figure 3H-H' and Supplemental Video 4**). Quantification of the *gap43*
503 reporter signal in single z-plane images from the medial TeO zone (**Figure 3A and 3B'-G'**)
504 showed that *gap43* reporter signal increased in the cTeO at 4 dpONC, peaked at 5 dpONC,
505 then diminished by 8-10 dpONC (**Figure 3J-K**; pre ONC vs 4 dpONC *P* value = 0.0446; pre
506 ONC vs 5 dpONC *P* value = 0.0346). No significant difference in the *gap43* reporter signal
507 was observed between males and females at any time-point tested (**Figure 3K**). In addition,

508 we observed a progression of the *gap43* reporter signal in the cTeO from a rostral to caudal
509 position over time (**Figure 3J, 3L and Supplemental Video 4**). While the downregulation of
510 *gap43* reporter signal correlated with results from the DLR assay which showed vision
511 recovery from 5-10 dpONC, the head tilt angle continued to improve after the complete
512 downregulation of *gap43* reporter signal expression (**Figure S5L**). We speculate that after
513 *gap43* reporter downregulation, additional modifications occur in the neuronal circuitry that
514 facilitate functional recovery. There was no significant upregulation of *gap43* reporter signal in
515 the ipsilateral optic tectum (iTeO) between pre ONC and 5 dpONC conditions (**Figure 3M-Q**),
516 suggesting a complete decussation of the optic nerve at the optic chiasm similar to that in
517 zebrafish (Diekmann et al., 2015). Taken together, we have generated a novel DC transgenic
518 line that takes advantage of the *gap43* promoter to visualize *in vivo* axon regeneration. When
519 combined with functional assays, this line has allowed us to correlate cellular phenotypes with
520 long distance RGC axon regeneration with vision recovery.
521
522 ***Regenerated axons display an altered arborization pattern post-ONC***
523 In pro-regenerative vertebrates, studies have shown that RGC axons re-innervate the TeO
524 after an optic nerve injury (Dow et al., 1994; Zou et al., 2013; Hu and Veldman, 2025).
525 However, it is unclear if RGC axons re-establish connections for functional vision recovery by
526 replicating their original axonal arborization pattern after injury. Imaging the brain of the same
527 animal before and after injury would help answer this question but this has not been feasible
528 using traditional adult animal models. To compare the arborization pattern of RGC axons in
529 the TeO before injury and post-regeneration, we used sparse labeling to visualize individual
530 cells by introducing mosaic expression of the *isl2b:TdTomato-caax* plasmid in *mitf*$^{-/-}$ fish. The
531 zebrafish *isl2b* promoter drives transgene expression in healthy RGCs (Ben Fredj et al., 2010).
532 We imaged the entire contralateral MB region of uninjured fish, subjected them to an ONC
533 injury, then imaged them throughout the regeneration process (**Figure 4A**). Compared to pre-
534 injury conditions, we observed degeneration of RGC axons at 1 dpONC as indicated by the
535 fragmentation and reduction of the *isl2b*-driven fluorescent signal in the TeO (**Figure 4B-C**

536 **and 4B'-C'**). By 5 dpONC, an extensive network of regenerating neurites was observed
537 (**Figure 4D and 4D'**). Post-regeneration, neuronal remodeling was observed between 5-10
538 dpONC (**Figure 4D-E and 4D'-E'**), corresponding to the time when gradual improvements in
539 the DLR were observed (**Figure 1D**). When detailed optical sectioning of the cTeO was
540 performed in the same animal before and after an ONC, and the mean intensity of the signal
541 was plotted by depth, a general similarity in the distribution of the re-innervated RGC axons
542 was observed (**Figure 4F-H, 5A-K and Supplemental Video 5**). Interestingly, axonal re-
543 modeling continued to occur from 25-40 dpONC, a time-point after injured fish exhibit a normal
544 DLR (**Figure 5G-K and 5J'-K'**). By comparing the patterning of RGC neurites before injury
545 and at 40 dpONC, we observed a stark difference in the dorsal cTeO (**Figure 5L**). When
546 imaging at a deeper medial level within the TeO, we observed the expanding arborization of
547 regenerating RGC axons from 10-40 dpONC, a period later than that in the dorsal TeO (**Figure**
548 **5G and 5M-P**). Similar to that in the dorsal TeO, the patterning of RGC axons in the deeper
549 medial zone of the TeO pre-injury was distinct from that at 40 dpONC (**Figure 5N**).
550
551 ***Myelinating oligodendrocyte membrane dynamics during RGC axon regeneration in the***
552 ***cTeO***
553 Myelination in the CNS has been well-documented using longitudinal imaging in developing
554 zebrafish larvae, owing to their optical transparency (Karttunen et al., 2017; Hughes and
555 Appel, 2020; Li et al., 2024). Based on fixed time-point histological data and results from
556 pooled tissue samples, it has been reported that adult zebrafish can restore myelin to full
557 thickness 4 weeks after a CNS injury (Münzel et al., 2014; Zou et al., 2015). To visualize
558 myelinating oligodendrocyte membrane dynamics and analyze the relationship between
559 myelin and regenerating neurites in adult DC *in vivo*, we generated a double transgenic line
560 *Tg(mbpa:TdTomato-CAAX, gap43:mGreenLantern-CAAX)* where both oligodendrocyte
561 membranes and regenerating neurites are fluorescently labeled. Following ONC, we observed
562 changes in the morphology of the oligodendrocyte membrane reporter signal (**Figure 6A-D,**
563 **6B'-D' and 6B''-D''**) and its pattern (**Figure 6G**), alongside changes in regenerating neurites

564 in the cTeO (**Figure 6B-D and 6B”-D”**). There was a significant decrease in the percentage
565 area covered by myelin in the cTeO at 5 dpONC compared to pre-injury levels (**Figure 6H**; pre
566 ONC vs 5 dpONC *P* value = 0.0055). At this time point, re-innervation of *gap43* positive axons
567 in the cTeO was observed (**Figure 6D and 6D”**), with some myelin fragments in contact with
568 regenerating neurites (**Figure S7A-C, 7B’-C’, 7B”-C” and Supplemental Video 6**). When
569 comparing the pre-injury state (**Figure 6B and 6B”**) to later post ONC time points, the myelin
570 pattern remained altered (**Figure 6E-F, 6E’-F’ and 6G**) and myelin levels remained reduced
571 (**Figure 6H**; pre ONC vs 40 dpONC *P* = 0.0065). Even at 60 dpONC, myelin patterns remained
572 distinct from that in the iTeO (**Figure S7D-F**). Although the *mbpa:TdTomato-CAAX*
573 oligodendrocyte membrane reporter labels both demyelinating myelin fragments and newly
574 formed myelin, we were able to detect demyelination and remyelination by comparing the
575 myelin pattern in the same region across different time points (**Figure 6I-L**).
576
577 In conclusion, our work demonstrates that with the development of unique transgenic lines,
578 robust longitudinal imaging techniques, and vision-based behavioral assays, adult DC can be
579 utilized for comprehensive studies that quantify and correlate CNS axon regeneration,
580 myelination, and functional recovery.
581
582 ***Discussion***
583 Many questions remain unanswered regarding the regeneration of axons in the CNS (Tsata
584 and Wehner, 2021). A major hurdle has been understanding how regenerating axons re-
585 innervate their targets in the process of reforming functional circuits. Observing this
586 phenomenon *in vivo* and identifying contributing cellular interactions is essential. Some
587 progress has been achieved by comparing the differential regenerative capacity of teleost fish
588 such as zebrafish and medaka (Lai et al., 2017; Lai et al., 2019; Shimizu and Kawasaki, 2021;
589 Chowdhury et al., 2022). However, a limitation to this approach is the inability to analyze the
590 contribution of dynamic spatio-temporal interactions between different cell types during CNS
591 regeneration and functional recovery. In this study, we have established a new adult animal

model, *Danionella cerebrum*, for the longitudinal study of CNS regeneration using the optic nerve crush injury. We harnessed the properties of their optical transparency and small size in adulthood and performed longitudinal *in vivo* imaging of cell specific fluorescent reporters throughout the injury and regeneration process. We demonstrated that adult DC possess the ability to regenerate their RGC axons following injury, ultimately leading to functional visual recovery. Imaging revealed that axons regenerated over a long distance and exhibited evidence of axonal remodeling. Real-time *in vivo* characterization of regeneration and recovery was facilitated by generating novel DC transgenic reporter lines for axonogenesis and myelinated oligodendrocyte membranes. For longitudinal assessment of RGCs pre- and post-regeneration, we employed a sparse labeling technique using an RGC specific promoter. CRISPR/Cas9 genome editing was used to generate a pigment mutant line to enhance *in vivo* brain imaging. Additionally, two behavior-based assays were developed to assess vision recovery. Using these tools, we found that through axon remodeling events, the regenerated axon network displayed an arborization pattern distinct from its pre-injury state and that regenerating axons re-innervated appropriate targets, leading to functional vision recovery. However, levels of myelin expression and its pattern of distribution were not fully restored even well after vision recovery. The DC model provides new avenues for future studies aimed at understanding how successful CNS regeneration is orchestrated.

The time course of axonal regeneration events in the TeO following optic nerve injury was illustrated using *Tg(gap43:mGreenLantern-CAAX)* and mosaic *isl2b:TdTomato-CAAX* expression experiments. While reporter expression driven by the *gap43* promoter is transiently upregulated in regenerating axons, it is not specific to RGCs. The *isl2b* promoter, on the other hand, drives reporter expression specifically in RGCs, regardless of injury. However, literature suggests that the *isl2b* gene is downregulated following optic nerve injury in other teleost fish (Chen et al., 2022; Ali et al., 2025). Due to this property, tectal denervation and reinnervation were not quantified using the *isl2b* promoter, as it is not possible to measure and compare reporter signal intensity within the same animal at different time points to reflect the extent of

620 RGC axon regeneration. Additionally, the transient and mosaic nature of *isl2b* reporter
621 expression used for sparse RGC labeling prevents reliable signal quantification across
622 animals. Given the distinct properties of the *gap43* and *isl2b* promoters, they complement
623 each other by enabling visualization of early axon regeneration and subsequent axon
624 reinnervation, respectively. In this study, the survival rate of RGCs in DC following ONC was
625 not characterized. We observed that the same labeled RGCs reinnervated the optic tectum
626 after ONC in the sparse and mosaic labeled *isl2b* reporter experiments. Due to the mosaic
627 nature of the labeling, the regenerating axons are likely derived from the injured *isl2b* reporter
628 expressing RGCs that were imaged prior to ONC. However, since an increase in the number
629 of RGCs throughout life has been reported in other teleost fish (Wan et al., 2016), future
630 studies are needed to characterize the contribution of newly formed RGCs to functional visual
631 recovery following optic nerve injury in adult DC.
632
633 To establish a functional connection, axons must form a specific pattern to ensure proper
634 target innervation (Gibson and Ma, 2011; Hasegawa and Kuwako, 2022). Since traditional
635 animal models provide limited *in vivo* optical access to monitor regenerating axons in mature
636 brains, little data is available to determine whether similar axonal re-arborization patterns are
637 important for vision recovery. We tested the hypothesis that vision recovery relies on the post
638 injury arborization patterns produced by regenerated axons matching their pre-injury state.
639 We performed longitudinal imaging on animals with mosaic RGC labeling, monitored the
640 progression of regenerating axons after injury, and compared arborization patterns between
641 pre- and post-injury states. After ONC, we observed Wallerian degeneration followed by re-
642 innervation of axons into the cTeO. Initially, regenerating axons formed an extensive network.
643 Later, at a phase coinciding with vision recovery, axon remodeling occurred. Intriguingly, when
644 comparing the axonal innervation in the same animal between the pre-injury state and the
645 remodeling phase, we observed a similar distribution of the re-innervated neurites within the
646 cTeO but with distinct arborization patterns. In conclusion, we demonstrated that RGC axons
647 can regenerate and re-innervate correct targets in the TeO, leading to vision recovery.

648

649 It remains unclear, however, whether all RGCs possess the same capacity for axon
650 regeneration. Studies using this sparse labeling approach in combination with specific
651 promoters for RGC subpopulations will provide insight into the capacity and necessity of
652 different RGC subtypes to regenerate in response to guidance molecules. Our work shows
653 that the DC model, combined with our transgenic lines and imaging methods, provides a
654 powerful platform for the *in vivo* investigation of mechanisms that regulate axonal arborization
655 pattern formation and refinement.

656

657 The relationship between myelination and regenerative outcomes remains unclear in adult
658 teleosts (Münzel et al., 2014; Karttunen et al., 2017). Our data revealed that injured animals
659 continued to exhibit reduced myelin levels in the cTeO even after vision recovery, suggesting
660 that although functional recovery occurs relatively quickly, a return to pre-injury myelin status
661 takes longer or may never be achieved. Although the DLR and LR assays provide information
662 on the intactness of the animal's vision, visual acuity remains untested. Our results suggest
663 that vision recovery occurs before the completion of remyelination. Further investigation is
664 needed to determine the relationship between visual acuity and remyelination. In the current
665 study, it remains unclear whether all regenerated RGC axons are re-myelinated and whether
666 the *mbpa:TdTomato-CAAX* oligodendrocyte membrane reporter labels compact myelin.
667 Future investigations using a combination of different RGC axon and myelin reporters along
668 with electron-microscopy and functional recovery assays, will provide insight into the role of
669 myelination in different stages of axonal regeneration and functional recovery.

670

671 The DC model serves as a novel system for uncovering the fundamental mechanisms
672 underlying CNS regeneration. It must be acknowledged that species-specific differences in
673 CNS regeneration capabilities and anatomical features between DC and humans exists.
674 Zebrafish have been proven to be a valuable translational research model (Phillips and

675 Westerfield, 2014) with 71.4% of human genes having at least one zebrafish orthologue (Howe
676 et al., 2013). A recent study suggested that 85% of zebrafish genes have a homolog in DC
677 (Schulze et al., 2018b), highlighting the translational potential of the DC model. Currently, 86%
678 of the DC genome is annotated (Kadobianskyi et al., 2019). Future efforts to continuously
679 improve the DC genome sequence and its annotation will facilitate transcriptomic analyses
680 and cross-species comparisons, enabling the identification of candidate pro-regenerative
681 pathways for further validation in non-regenerative models.
682
683 Together, the arsenal of adult transgenic live imaging tools and visual functional recovery
684 assays established in this study create a powerful and unique opportunity for the utilization of
685 DC to study optic nerve regeneration. Our transgenic lines, combined with functional recovery
686 assays, hold promise for advancing our understanding of how the nervous system is
687 successfully rewired after injury and for gaining insight into how this process is regulated
688 across diverse contexts — including, but not limited to, brain stab injuries, spinal cord injuries,
689 and other injuries to sensory systems such as olfactory and auditory systems.
690

691 ***Acknowledgements***

692 Wild-type DC stocks were obtained from the laboratory of Dr. Adam Douglass (University of
693 Utah). The *gap43* promoter containing plasmid *pW1GFG43SA* was a kind gift from Dr. Ava
694 Udvadia (University of Wisconsin). Dr. Ross Collery (Medical College of Wisconsin) cloned
695 the *pME-mGreenLantern* construct. Hannah G. Tebbs (Medical College of Wisconsin)
696 performed the LR reaction and purified the *gap43:mGreenLantern-CAAX* construct. This work
697 is funded by the National Institutes of Health Office of the Director under Award Number
698 R21OD033664 (P.Y.L.), S10OD032136 (to Brandon Tefft - MCW engineering core), and the
699 Advancing a Healthier Wisconsin Endowment (P.Y.L). Portions of the schematic diagrams
700 were created using BioRender (BioRender.com).
701

702 ***Author contributions***

703 M.M. and P.Y.L. conceptualized and designed the experiments, interpreted the results, wrote
704 and revised the manuscript with input from all authors. M.M, J.L.A, N.R.W. and J.A.P.
705 performed the experiments, analyzed the results and wrote the Materials and Methods
706 section. M.B.V. generated the *gap43:mGreenLantern-CAAX* plasmid and assisted in
707 establishing the ONC technique and the DLR assay.
708
709 ***Conflicting Interest:*** All authors declare no competing interests.
710
711 ***Data and materials availability:*** Materials (including transgenic lines and plasmids), as well
712 as the data supporting this study are available from the corresponding author upon request.
713
714 ***References***

715 Ali A, Schriever H, Kostka D, Kuwajima T, Koenig KM, Gross J (2025) Zebrafish optic nerve
716 injury results in systemic retinal ganglion cell dedifferentiation.
717 bioRxiv:2025.2004.2009.646875.

718 Beckers A, Bergmans S, Van Dyck A, Moons L (2023) Analysis of Visual Recovery After
719 Optic Nerve Crush in Adult Zebrafish. Methods Mol Biol 2636:437-447.

720 Belin S, Nawabi H, Wang C, Tang S, Latremoliere A, Warren P, Schorle H, Uncu C, Woolf
721 CJ, He Z, Steen JA (2015) Injury-induced decline of intrinsic regenerative ability
722 revealed by quantitative proteomics. Neuron 86:1000-1014.

723 Ben Fredj N, Hammond S, Otsuna H, Chien CB, Burrone J, Meyer MP (2010) Synaptic
724 activity and activity-dependent competition regulates axon arbor maturation, growth
725 arrest, and territory in the retinotectal projection. J Neurosci 30:10939-10951.

726 Bormann P, Zumsteg VM, Roth LW, Reinhard E (1998) Target contact regulates GAP-43 and
727 alpha-tubulin mRNA levels in regenerating retinal ganglion cells. J Neurosci Res
728 52:405-419.

729 Britz R, Conway KW, Rüber L (2021) The emerging vertebrate model species for
730 neurophysiological studies is Danionella cerebrum, new species (Teleostei:
731 Cyprinidae). Sci Rep-Uk 11:18942-18942.

732 Campbell BC, Nabel EM, Murdock MH, Lao-Peregrin C, Tsoulfas P, Blackmore MG, Lee FS,
733 Liston C, Morishita H, Petsko GA (2020) mGreenLantern: a bright monomeric
734 fluorescent protein with rapid expression and cell filling properties for neuronal
735 imaging. Proc Natl Acad Sci U S A 117:30710-30721.

736 Chato-Astrain J, García-García ÓD, Campos F, Sánchez-Porras D, Carriel V (2022) Basic
737 Nerve Histology and Histological Analyses Following Peripheral Nerve Repair and
738 Regeneration. In: Peripheral Nerve Tissue Engineering and Regeneration (Phillips

JB, Hercher D, Hausner T, eds), pp 151-187. Cham: Springer International Publishing.

Chen S, Lathrop KL, Kuwajima T, Gross JM (2022) Retinal ganglion cell survival after severe optic nerve injury is modulated by crosstalk between Jak/Stat signaling and innate immune responses in the zebrafish retina. Development 149.

Chowdhury K, Lin S, Lai SL (2022) Comparative Study in Zebrafish and Medaka Unravels the Mechanisms of Tissue Regeneration. Frontiers in Ecology and Evolution 10.

Cook V, Groneberg AH, Hoffmann M, Kadobianskyi M, Veith J, Schulze L, Henninger J, Britz R, Judkewitz B (2024) Ultrafast sound production mechanism in one of the smallest vertebrates. Proc Natl Acad Sci U S A 121:e2314017121.

Daeschler SC, Zhang J, Gordon T, Borschel GH (2022) Optical tissue clearing enables rapid, precise and comprehensive assessment of three-dimensional morphology in experimental nerve regeneration research. Neural Regen Res 17:1348-1356.

Diekmann H, Kalbhen P, Fischer D (2015) Characterization of optic nerve regeneration using transgenic zebrafish. Front Cell Neurosci 9:118.

Dow KE, Levine RL, Solc MA, DaSilva O, Riopelle RJ (1994) Axonal transport of proteoglycans in regenerating goldfish optic nerve. Exp Neurol 126:129-137.

Dunn TW, Gebhardt C, Naumann EA, Riegler C, Ahrens MB, Engert F, Del Bene F (2016) Neural Circuits Underlying Visually Evoked Escapes in Larval Zebrafish. Neuron 89:613-628.

Gibson DA, Ma L (2011) Developmental regulation of axon branching in the vertebrate nervous system. Development 138:183-195.

Groneberg AH, Dressler LE, Kadobianskyi M, Muller J, Judkewitz B (2024) Development of sound production in Danionella cerebrum. J Exp Biol 227.

Hall TE, Martel N, Ariotti N, Xiong Z, Lo HP, Ferguson C, Rae J, Lim YW, Parton RG (2020) In vivo cell biological screening identifies an endocytic capture mechanism for T-tubule formation. Nat Commun 11:3711.

Hasegawa K, Kuwako K-i (2022) Molecular mechanisms regulating the spatial configuration of neurites. Seminars in Cell & Developmental Biology 129:103-114.

Hecker A, Anger P, Braaker PN, Schulze W, Schuster S (2020) High-resolution mapping of injury-site dependent functional recovery in a single axon in zebrafish. Communications Biology 3:307.

Howe K et al. (2013) The zebrafish reference genome sequence and its relationship to the human genome. Nature 496:498-503.

Hu M, Veldman MB (2025) Srebf2 mediates successful optic nerve axon regeneration via the mevalonate synthesis pathway. Molecular Neurodegeneration 20:28.

Hughes AN, Appel B (2020) Microglia phagocytose myelin sheaths to modify developmental myelination. Nat Neurosci 23:1055-1066.

Jung SH, Kim S, Chung AY, Kim HT, So JH, Ryu J, Park HC, Kim CH (2010) Visualization of myelination in GFP-transgenic zebrafish. Dev Dyn 239:592-597.

Kadobianskyi M, Schulze L, Schuelke M, Judkewitz B (2019) Hybrid genome assembly and annotation of Danionella translucida. Scientific Data 6:156.

Kang H (2021) Sample size determination and power analysis using the G*Power software. J Educ Eval Health Prof 18:17.

Karimi-Abdolrezaee S, Verge VM, Schreyer DJ (2002) Developmental down-regulation of GAP-43 expression and timing of target contact in rat corticospinal neurons. Exp Neurol 176:390-401.

Karttunen MJ, Czopka T, Goedhart M, Early JJ, Lyons DA (2017) Regeneration of myelin sheaths of normal length and thickness in the zebrafish CNS correlates with growth of axons in caliber. PLoS One 12:e0178058.

Kwan KM, Fujimoto E, Grabher C, Mangum BD, Hardy ME, Campbell DS, Parant JM, Yost HJ, Kanki JP, Chien CB (2007) The Tol2kit: a multisite gateway-based construction kit for Tol2 transposon transgenesis constructs. Dev Dyn 236:3088-3099.

Labun K, Montague TG, Gagnon JA, Thyme SB, Valen E (2016) CHOPCHOP v2: a web tool for the next generation of CRISPR genome engineering. Nucleic Acids Res 44:W272-276.

Labun K, Montague TG, Krause M, Torres Cleuren YN, Tjeldnes H, Valen E (2019) CHOPCHOP v3: expanding the CRISPR web toolbox beyond genome editing. Nucleic Acids Res 47:W171-W174.

Lai SL, Marín-Juez R, Stainier DYR (2019) Immune responses in cardiac repair and regeneration: a comparative point of view. Cell Mol Life Sci 76:1365-1380.

Lai SL, Marín-Juez R, Moura PL, Kuenne C, Lai JKH, Tsedeke AT, Guenther S, Looso M, Stainier DY (2017) Reciprocal analyses in zebrafish and medaka reveal that harnessing the immune response promotes cardiac regeneration. Elife 6.

Lam PY (2022) Longitudinal in vivo imaging of adult Danionella cerebrum using standard confocal microscopy. Dis Model Mech 15.

Lambert CJ, Freshner BC, Chung A, Stevenson TJ, Bowles DM, Samuel R, Gale BK, Bonkowsky JL (2018) An automated system for rapid cellular extraction from live zebrafish embryos and larvae: Development and application to genotyping. PLoS One 13:e0193180.

Lee TJ, Briggman KL (2023) Visually guided and context-dependent spatial navigation in the translucent fish Danionella cerebrum. Curr Biol 33:5467-5477 e5464.

Li J, Miramontes TG, Czopka T, Monk KR (2024) Synaptic input and Ca2+ activity in zebrafish oligodendrocyte precursor cells contribute to myelin sheath formation. Nature Neuroscience 27:219-231.

Lim JH, Stafford BK, Nguyen PL, Lien BV, Wang C, Zukor K, He Z, Huberman AD (2016) Neural activity promotes long-distance, target-specific regeneration of adult retinal axons. Nat Neurosci 19:1073-1084.

Lindemann N, Kalix L, Possiel J, Stasch R, Kusian T, Koster RW, von Trotha JW (2022) A comparative analysis of Danionella cerebrum and zebrafish (Danio rerio) larval locomotor activity in a light-dark test. Front Behav Neurosci 16:885775.

Lindsey AE, Powers MK (2007) Visual behavior of adult goldfish with regenerating retina. Vis Neurosci 24:247-255.

Lister JA, Robertson CP, Lepage T, Johnson SL, Raible DW (1999) nacre encodes a zebrafish microphthalmia-related protein that regulates neural-crest-derived pigment cell fate. Development 126:3757-3767.

Lowe DG (2004) Distinctive image features from scale-invariant keypoints. International journal of computer vision 60:91-110.

McKee A, McHenry MJ (2020) The Strategy of Predator Evasion in Response to a Visual Looming Stimulus in Zebrafish (Danio rerio). Integr Org Biol 2:obaa023.

Mensinger AF, Powers MK (2007) Visual function in regenerating teleost retina following surgical lesioning. Vis Neurosci 24:299-307.

Montague TG, Cruz JM, Gagnon JA, Church GM, Valen E (2014) CHOPCHOP: a CRISPR/Cas9 and TALEN web tool for genome editing. Nucleic Acids Res 42:W401-407.

Münzel EJ, Becker CG, Becker T, Williams A (2014) Zebrafish regenerate full thickness optic nerve myelin after demyelination, but this fails with increasing age. Acta Neuropathol Commun 2:77.

Murashova L, Dyachuk V (2025) Modeling traumatic brain and neural injuries: insights from zebrafish. Front Mol Neurosci 18:1552885.

Nevin LM, Robles E, Baier H, Scott EK (2010) Focusing on optic tectum circuitry through the lens of genetics. BMC Biol 8:126.

Oehlers SH, Cronan MR, Scott NR, Thomas MI, Okuda KS, Walton EM, Beerman RW, Crosier PS, Tobin DM (2015) Interception of host angiogenic signalling limits mycobacterial growth. Nature 517:612-615.

Park KK, Liu K, Hu Y, Smith PD, Wang C, Cai B, Xu B, Connolly L, Kramvis I, Sahin M, He Z (2008) Promoting axon regeneration in the adult CNS by modulation of the PTEN/mTOR pathway. Science 322:963-966.

Penalva-Tena A, Bedke J, Gaudin A, Barrios JP, Bertram EPL, Douglass AD Oxytocin-mediated social preference and socially reinforced reward learning in the miniature fish Danionella cerebrum. Current Biology.

Penalva A, Bedke J, Cook ESB, Barrios JP, Bertram EP, Douglass AD (2018) Establishment of the miniature fish species Danionella translucida as a genetically and optically tractable neuroscience model. bioRxiv.

Phillips JB, Westerfield M (2014) Zebrafish models in translational research: tipping the scales toward advancements in human health. Dis Model Mech 7:739-743.

855 Pinzon-Olejua A, Welte C, Chekuru A, Bosak V, Brand M, Hans S, Stuermer CA (2017) Cre-
856 inducible site-specific recombination in zebrafish oligodendrocytes. Dev Dyn 246:41-
857 49.

858 Rajan G, Lafaye J, Faini G, Carbo-Tano M, Duroure K, Tanese D, Panier T, Candelier R,
859 Henninger J, Britz R, Judkewitz B, Gebhardt C, Emiliani V, Debregeas G, Wyart C,
860 Del Bene F (2022) Evolutionary divergence of locomotion in two related vertebrate
861 species. Cell Rep 38:110585.

862 Reinhard E, Nedivi E, Wegner J, Skene JH, Westerfield M (1994) Neural selective activation
863 and temporal regulation of a mammalian GAP-43 promoter in zebrafish.
864 Development 120:1767-1775.

865 Schaeffer J, Vilallongue N, Belin S, Nawabi H (2023) Axon guidance in regeneration of the
866 mature central nervous system: step by step. Neural Regeneration Research
867 18:2665-2666.

868 Schindelin J, Arganda-Carreras I, Frise E, Kaynig V, Longair M, Pietzsch T, Preibisch S,
869 Rueden C, Saalfeld S, Schmid B (2012) Fiji: an open-source platform for biological-
870 image analysis. Nature methods 9:676-682.

871 Schulze L, Henninger J, Kadobianskyi M, Chaigne T, Faustino AI, Hakiy N, Albadri S,
872 Schuelke M, Maler L, Del Bene F, Judkewitz B (2018a) Transparent Danionella
873 translucida as a genetically tractable vertebrate brain model. Nat Methods 15:977-
874 983.

875 Schulze L, Henninger J, Kadobianskyi M, Chaigne T, Faustino AI, Hakiy N, Albadri S,
876 Schuelke M, Maler L, Del Bene F, Judkewitz B (2018b) Transparent Danionella
877 translucida as a genetically tractable vertebrate brain model. Nature Methods 15:977-
878 983.

879 Shimizu Y, Kawasaki T (2021) Differential Regenerative Capacity of the Optic Tectum of
880 Adult Medaka and Zebrafish. Front Cell Dev Biol 9:686755.

881 Suthya AR, Wong CHY, Bourne JH (2024) Diving head-first into brain intravital microscopy.
882 Front Immunol 15:1372996.

883 Temizer I, Donovan JC, Baier H, Semmelhack JL (2015) A Visual Pathway for Looming-
884 Evoked Escape in Larval Zebrafish. Curr Biol 25:1823-1834.

885 Thuma TBT, Bogovic JA, Gunton KB, Jimenez H, Negreiros B, Pulido JS (2023) The big
886 warp: Registration of disparate retinal imaging modalities and an example overlay of
887 ultrawide-field photos and en-face OCTA images. PLoS One 18:e0284905.

888 Tsata V, Wehner D (2021) Know How to Regrow-Axon Regeneration in the Zebrafish Spinal
889 Cord. Cells 10.

890 Udvadia AJ (2008) 3.6 kb genomic sequence from Takifugu capable of promoting axon
891 growth-associated gene expression in developing and regenerating zebrafish
892 neurons. Gene Expr Patterns 8:382-388.

893 Vasconcelos RO, Bolgan M, Matos AB, Van-Dunem SP, Penim J, Amorim MCP (2024)
894 Characterization of the vocal behavior of the miniature and transparent fish model,
895 Danionella cerebruma). J Acoust Soc Am 155:781-789.

896 Veith J, Chaigne T, Svanidze A, Dressler LE, Hoffmann M, Gerhardt B, Judkewitz B (2024)
897 The mechanism for directional hearing in fish. Nature 631:118-124.

898 Wan Y, Almeida AD, Rulands S, Chalour N, Muresan L, Wu Y, Simons BD, He J, Harris WA
899 (2016) The ciliary marginal zone of the zebrafish retina: clonal and time-lapse
900 analysis of a continuously growing tissue. Development 143:1099-1107.

901 Watanabe S, Takabayashi A, Takagi S, von Baumgarten R, Wetzig J (1989) Dorsal light
902 response and changes of its responses under varying acceleration conditions. Adv
903 Space Res 9:231-240.

904 Williams PR, Benowitz LI, Goldberg JL, He Z (2020) Axon Regeneration in the Mammalian
905 Optic Nerve. Annu Rev Vis Sci 6:195-213.

906 Zada D, Schulze L, Yu JH, Tarabishi P, Napoli JL, Milan J, Lovett-Barron M (2024)
907 Development of neural circuits for social motion perception in schooling fish. Curr
908 Biol 34:3380-3391 e3385.

909 Zou S-q, Yin W, Huang Y-b, Tian C, Ge S-c, Hu B (2015) Chapter 2 - Functional
910 Regeneration and Remyelination in the Zebrafish Optic Nerve. In: Neural
911 Regeneration (So K-F, Xu X-M, eds), pp 21-41. Oxford: Academic Press.

912 Zou S, Tian C, Ge S, Hu B (2013) Neurogenesis of retinal ganglion cells is not essential to
913 visual functional recovery after optic nerve injury in adult zebrafish. PLoS One
914 8:e57280.

915

916 ***Main figure titles and legends***

917 **Figure 1. Assessing functional recovery after an ONC using DLR and LR Assays. (A)**
918 Dorsal view of an adult DC pre ONC with black arrowheads flanking the optic nerve. **(A')**
919 Schematic representation of the black dotted area in (A) illustrating the ONC procedure. After
920 a successful ONC, the region of the optic nerve subjected to ONC turns opaque. **(B)**
921 Schematic representation the DLR assay chamber. **(B')** Illustration of how the head tilt angle
922 is measured. Brown arrow showing a right tilt (positive angle) and green arrow showing a left
923 tilt (negative angle). **(C)** Timeline schematic of the DLR assay with the time-points that head
924 tilt angle was measured indicated by black dots. (i-iii) Representative images of the same fish
925 (i) pre ONC, and at (ii) 1 dpONC and (iii) 18 dpONC. Scale bar = 200 µm. **(D)** Change in head
926 tilt angle compared to pre ONC values. All data are represented in mean ± Standard Error of
927 Mean (±SEM). Black solid line represents all animals (n = 18), pink dotted line represents
928 females (n = 9), and blue dotted line represents males (n = 9). *P* values were calculated using

929 Mixed Effects Repeated Measures 2-way ANOVA. *P* values of all animals (total) of each time-
930 points are indicated above the trace where pre and post ONC measurements were compared.
931 *P* values from left to right: $P < 0.0001$, $P < 0.0001$, $P < 0.0001$, $P < 0.0001$, $P < 0.0001$, $P =$
932 0.0105, and $P = 0.1088$. For females vs. males, at 1 dpONC, $P = 0.0655$; at 4 dpONC, $P =$
933 0.3086; at 6 dpONC, $P = 0.6475$; at 8 dpONC, $P = 0.6981$; at 10 dpONC $P = 0.0449$; at 14
934 dpONC $P = 0.7762$; and 18 dpONC $P = 0.9985$. Annotations as presented on graph: ns (not
935 significant) $P \geq 0.05$, * $P < 0.05$, ** $P < 0.01$, *** $P < 0.001$, **** $P < 0.0001$. **(E)** Schematic
936 representation of the LR Assay. **(F)** Schematic illustration of the expanding circle parameters
937 used in the LR assay. **(G)** Timeline schematic of the LR assay with the time-points that LR was
938 assessed indicated by black dots. **(H)** Percentage of fish responding to the LR stimulus pre-
939 and post-injury. All data represented in mean ±SEM (n = 14 including 7 females and 7 males).
940 *P* value of each time-point was calculated using Repeated Measures 1-way ANOVA. *P* values
941 represented as compared to -1 dpONC/pre-injury time-point. *P* values from left to right: $P =$
942 0.5013, $P < 0.0001$, $P = 0.0017$, $P = 0.1126$, and $P = 0.7827$. Annotations as presented on
943 graph: ns $P \geq 0.05$, ** $P < 0.01$, **** $P < 0.0001$.
944
945 **Figure 2. Generating the *Tg(gap43:mGreenLantern-CAAX)* axonogenesis reporter line.**
946 **(A-D)** and **(A'-D')** Confocal images of *Tg(gap43:mGreenLantern-CAAX)* larvae acquired using
947 a 20X objective (N.A. = 0.75, 0.9 µm/step). **(A-D)** *gap43* promoter driven expression (green
948 channel) overlayed with the bright field (BF) channel in 2 and 5 dpf larvae. **(A-A' and C-C')**
949 Dorsal confocal MIP images. The total z-stack was 199.80 µm in (A-A') and 246.60 µm in (C-
950 C'). (B-B' and D-D') Lateral confocal MIP images. The total z-stack was 199.90 µm in (B-B')
951 and 199.80 µm in (D-D'). (B'') Inset of the region marked in the blue rectangle in B' showing
952 *gap43*-driven expression of fluorescent protein in the eye. **(E-E')** Lateral confocal MIP images
953 of an adult *Tg(gap43:mGreenLantern-CAAX)* male at 2.5 mpf. Image was acquired using a
954 4X objective (N.A. = 0.2). The total z-stack was 1050 µm with a 25 µm/step. ♂ = Male. **(E)**
955 *gap43* promoter driven expression (green channel) overlayed with the BF channel. **(E')** Green
956 channel only. **(F)** Schematic representation of the approach used to acquire confocal images

957 of the adult DC brain (images shown in G-I and G'-I'). Z-stacks were acquired at 2.5 μm/z-step
958 using a 10X objective (N.A. = 0.45) on a 2 mpf *Tg(gap43:mGreenLantern-CAAX)* male
959 measuring 1.32 cm in length. **(G-I)** *gap43* promoter driven expression (green channel)
960 overlayed with the bright field (BF) channel. **(G'-I')** Green channel only. **(G and G')** Single
961 plane image of the dorsal brain (z-position= 0.00 μm). **(H-H')** Single plane image of the medial
962 brain (z-position = 100.00 μm). **(I-I')** Single plane image of the ventral brain (z-position =
963 200.00 μm).
964
965 **Figure 3. Longitudinal confocal imaging of axon regeneration after an ONC injury.**
966 **(A)** Schematic illustrations showing the imaged area depicted in B-G and B'-G'. The solid
967 green rectangle in the lateral view (a), corresponds to the area imaged and presented as MIPs
968 of the dorsal portion of the TeO in B-G. The green dotted line in the lateral view (b),
969 corresponds to an area more ventral to (a) and presented as single plane images of the medial
970 TeO in B'-G'. ♂ = Male. **(B-G, B'-G', B"-G")** Confocal images acquired in a
971 *Tg(gap43:mGreenLantern-CAAX)* male *in mitf*$^{-/-}$ at 3 mpf with a length of 1.36 cm using a 20X
972 objective (N.A. = 0.75, 0.9 μm/z-step). **(B-G)** Dorsal TeO MIP images of the *gap43* promoter-
973 driven fluorescent signal at the indicated time-points. The total z-stack thickness was 117.00
974 μm in (B), 115.20 μm in (C), 119.70 μm in (D), 112.50 μm in (E), 115.20 μm in (F), and 118.80
975 μm in (G). **(B'-G')** Single plane images of a deeper medial region in the TeO of the same fish.
976 **(B"-G")** Magnified area corresponding to the yellow dotted rectangle in B'-G'. Measurements
977 of *gap43* reporter signal were made in the region bounded by the white dotted lines. **(H)**
978 Magnified view of the region indicated by a blue rectangle in D. **(I)** Magnified view of the region
979 indicated by a blue rectangle in E. **(J)** *gap43* reporter signal intensity was quantified in the
980 area indicated by the white dotted line. This area represents the site of re-innervation (marked
981 by black arrow). **(K)** Mean intensity of *gap43* reporter expression in the ROI indicated in (J)
982 normalized to pre ONC levels was measured for 10 dpONC. All data represented in mean
983 ±SEM. Black line represents all animals (n = 16), pink dotted line represents the females (n =
984 7), blue dotted line represents the males (n = 9). *P* values at each time-point compared to pre

985 ONC were calculated using Mixed Effects Repeated Measures 2-way ANOVA. *P* values of all
986 animals (total) from left to right: *P* = 0.9728, *P* = 0.0446, *P* = 0.0346, *P* = 0.1417, *P* = 0.5474,
987 *P* = 0.9576. For females vs males, at 1 dpONC, *P* = 0.3399; at 4 dpONC, *P* = 0.3250; at 5
988 dpONC, *P* = 0.6274; at 6 dpONC, *P* = 0.5323; at 8 dpONC *P* = 0.8613; and at 10 dpONC *P* =
989 0.9375. Annotations as presented on graph: ns *P* ≥ 0.05, * *P* < 0.05. **(L)** Intensity of *gap43*
990 reporter signal (arbitrary units) in the TeO ROI (indicated in J) measured in the same animal
991 at the time-points indicated. **(M)** Schematic representation of regions and depths imaged in N-
992 P. Magenta rectangle in the dorsal view shows the region imaged in (N) and the dotted
993 rectangle shows the region in O-P. (a') Solid bar corresponds to the region imaged and shown
994 in (N) as a MIP. (b') Dotted line corresponds to the single plane images shown in (O-P). **(N-P)**
995 Confocal images acquired using a 10X objective (N.A. = 0.45, 2.5 μm/z-step) in a *mitf*$^{-/-}$
996 *Tg(gap43:mGreenLantern-CAAX)* male at 3.5 mpf with a length of 1.30 cm. White dotted line
997 separates the cTeO and the iTeO. **(N)** Dorsal TeO MIP image of the expression of *gap43*
998 reporter at 5 dpONC. The total z-stack thickness was 125.00 μm. **(O-P)** Medial TeO single z-
999 plane image of the expression of *gap43* reporter at time-points indicated. The ROI quantified
1000 in Q is demarked by the orange dotted lines. **(Q)** Intensity of *gap43* reporter expression
1001 normalized to pre ONC levels in the ROI indicated in (O-P). All data represented in mean
1002 ±SEM (n = 12). *P* values calculated using Repeated Measures 2-way ANOVA. For pre ONC,
1003 iTeO vs cTeO *P* > 0.9999; for 5 dpONC, iTeO vs cTeO *P* < 0.0001; for iTeO, pre ONC vs 5
1004 dpONC *P* = 0.9349; for cTeO; and pre ONC vs 5 dp ONC *P* < 0.0001. Annotations as presented
1005 on graph: ns *P* ≥ 0.05, **** *P* < 0.0001.
1006
1007 **Figure 4. Assessing retinal ganglion cell axon degeneration and regeneration using a**
1008 **sparse labeling technique.**
1009 **(A)** Schematic representation of regions imaged and shown in B-E and B'-E'. (a) Red dotted
1010 rectangle corresponds to the dorsal TeO area imaged and shown as a MIP in B-E and B'-E'.
1011 (b) Solid brown line indicates the position within the TeO imaged and shown as a single z-
1012 plane image in F-H. ♂ = Male. **(B-E)** and **(B'-E')** All images were acquired using a 40X

1013 objective (N.A. = 1.15, 0.4 μm/z-step) in a male *mitf*$^{-/-}$ fish at 2.5 mpf 1.34 cm in length with
1014 mosaic *isl2b:TdTomato-CAAX* expression. The total z-stack thickness used for MIP was 112
1015 μm. **(B-E)** MIP images showing the mosaic expression of *isl2b:TdTomato-CAAX* (magenta)
1016 combined with the corresponding bright field (BF) image in the dorsal region of the TeO at the
1017 time-points indicated. Dotted line in (C) indicates the location of the darker shade neuronal
1018 debris accumulation in the cTeO at 1 dpONC. **(B'-E')** Grey scale images of B-E with look-up
1019 tables (LUTs) shown in the upper right inset. **(i-viii)** Magnified view of regions of interest as
1020 indicated by rectangles in B'-E'. Green and yellow arrows highlight degenerating
1021 *isl2b:TdTomato-CAAX* expressing neurites. Green asterisks highlight remodeling of
1022 *isl2b:TdTomato-CAAX* expressing neurites. **(F-H)** Single z-plane images of medial TeO region
1023 showing the mosaic expression of *isl2b:TdTomato-CAAX* (magenta) combined with the
1024 corresponding bright field (BF) image at the time-points indicated. Dotted line indicates the
1025 area of the TeO where *isl2b:TdTomato-CAAX* expressing neurons are innervating. Images
1026 were acquired using a 20X objective lens (N.A. = 0.75).
1027
1028 **Figure 5. Longitudinal assessment of the re-innervation patterning of RGC axons pre-**
1029 **and post ONC.**
1030 **(A)** Schematic representation of the lateral view of the *D. cerebrum* brain where the blue box
1031 represents the region imaged, three-dimensionally (3-D) rendered, and presented in B-C. ♂ =
1032 Male. **(B-C and H-Q)** Images were acquired using a 40X objective (N.A. = 1.15, 0.4 μm/z-
1033 step) in a male *mitf*$^{-/-}$ fish at 2.5 mpf and 1.36 cm in length with mosaic *isl2b:TdTomato-CAAX*
1034 expression. **(B-C)** Color coded 3-D rendered images of mosaic *isl2b:TdTomato-CAAX*
1035 expression at pre ONC and 25 dpONC. The total z-stack thickness was 125.6 μm and imaging
1036 z-depth is indicated in the scale. (a') and (b') Represent the z-depth region shown in the MIP
1037 images of (H-L) and (M-Q), respectively. **(D)** Schematic representation of the dorsal and lateral
1038 view of the ROI used for calculating the mean *isl2b:TdTomato-CAAX* signal intensity in E-F on
1039 the confocal images shown in B-C, respectively. **(E-F)** Mean *isl2b:TdTomato-CAAX* signal
1040 intensity in the ROI at different z-depths at the time-points indicated. **(G)** Schematic

representation of regions imaged and shown in H-Q. The orange rectangle (a') indicates the region shown H-K and the black rectangle (b') indicates the region shown in M-P. **(H-K)** MIPs of the dorsal TeO region before ONC injury and at the time-points indicated. The total z-stack depth was 72.4 µm. Yellow boxes are magnified ROIs (J' and K'). Grey scale images with LUTs shown in the upper right inset. Pink asterisks = remodeling of *isl2b:TdTomato-CAAX* expressing neurites. **(L)** Overlay of pre ONC (yellow) and 40 dpONC (magenta) images. **(M-P)** MIPs of a deeper medial TeO region before ONC injury and at the time-points indicated. The total z-stack depth was 25.6 µm. Grey scale images with LUTs shown in the upper right inset. Dotted green oval = re-forming arbor field. Blue asterisks = remodeling of *isl2b:TdTomato-CAAX* expressing neurites. **(Q)** Overlay of pre ONC (yellow) and 40 dpONC (magenta) image.

Figure 6. Correlating RGC axonal regeneration with oligodendrocyte membrane reporter expression in the TeO after an ONC.

(A) Schematic representation of area imaged in B-F, B'-F' and B''-F'' is indicated by the brown rectangles in the dorsal and lateral view. Images were acquired then presented as MIPs with a 40X objective (N.A. = 1.15, 0.4 µm/z-step) in a double transgenic female *Tg(mbpa:TdTomato-CAAX, gap43:mGreenLantern-CAAX)* at 2.5 mpf and 1.37 cm in length. ♀ = female **(B-F)** Merged fluorescent signals from the myelin reporter (magenta) and the gap43 reporter (green) at the time-points indicated. **(B'-F')** Myelin reporter (magenta) only. LUTs shown in the upper right inset. (**B''-F'')** gap43 reporter (green) only. **(G)** Mean intensity of myelin signal under a line-ROI extending from the medial to lateral cTeO as indicated in B', D' and F'. **(H)** Percentage area covered by *mbpa:TdTomato-CAAX* signal in a fixed ROI in the cTeO. Data represented as mean ±SEM from 3 animals (2 males and 1 female). *P* values were calculated using 1-way ANOVA (pre vs 1 dpONC $P = 0.9987$; pre ONC vs 5 dpONC $P = 0.0055$; pre ONC vs. 10 dpONC $P = 0.0099$ and pre ONC vs 40 dpONC $P = 0.0065$). Annotations as presented on graph: ns $P \geq 0.05$, ** $P < 0.01$. **(I)** Schematic representation of the ROI imaged in a double transgenic male *Tg(mbpa:TdTomato-CAAX,*

1069 *gap43:mGreenLantern-CAAX)* fish, 2.5 mpf with a length of 1.27 cm, that was subjected to an
1070 ONC injury. Confocal images presented as MIPs in J-K. ♂ = male. **(J-K)** All images were
1071 acquired using a 40X objective (N.A. = 1.15, 0.4 μm/z-step). The total z-stack thickness was
1072 33.33 μm. **(J)** Signal from the myelin reporter in the cTeO region at 17 dpONC presented in
1073 greyscale. **(K)** The same region from the same fish was imaged at 22 dpONC. (White arrows
1074 = myelin fragments). **(L)** Overlay image of remyelination (magenta; fluorescent signal
1075 subtraction of area shown in J from K) and 22 dpONC (gray scale).

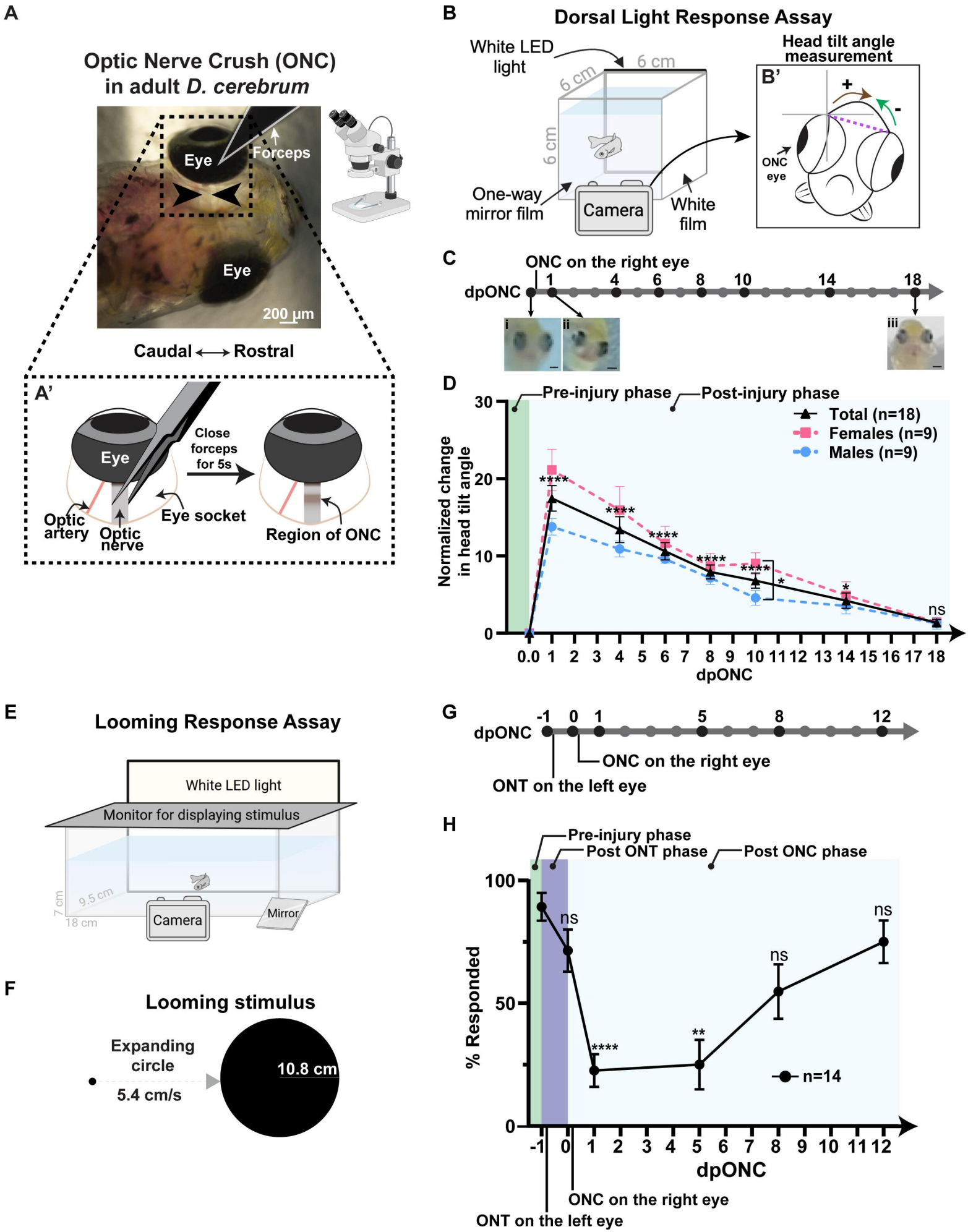
A
Optic Nerve Crush (ONC) in adult D. cerebrum
Eye
Forceps
Eye
200 µm
Caudal ⟷ Rostral
A'
Eye
Close forceps for 5s
Optic artery
Optic nerve
Eye socket
Region of ONC
B
Dorsal Light Response Assay
White LED light
6 cm
6 cm
6 cm
One-way mirror film
Camera
White film
Head tilt angle measurement
B'
+
-
ONC eye
C
ONC on the right eye
dpONC
1
4
6
8
10
14
18
i
ii
iii
D
Pre-injury phase
Post-injury phase
Total (n=18)
Females (n=9)
Males (n=9)
Normalized change in head tilt angle
30
20
10
0
****
****
****
****
****
*
*
ns
0.0 1 2 3 4 5 6 7 8 9 10 11 12 13 14 15 16 17 18
dpONC
E
Looming Response Assay
White LED light
Monitor for displaying stimulus
7 cm
9.5 cm
18 cm
Camera
Mirror
F
Looming stimulus
Expanding circle
5.4 cm/s
10.8 cm
G
dpONC
-1
0
1
5
8
12
ONC on the right eye
ONT on the left eye
H
Pre-injury phase
Post ONT phase
Post ONC phase
% Responded
100
50
0
ns
****
**
ns
ns
n=14
-1 0 1 2 3 4 5 6 7 8 9 10 11 12
dpONC
ONC on the right eye
ONT on the left eye

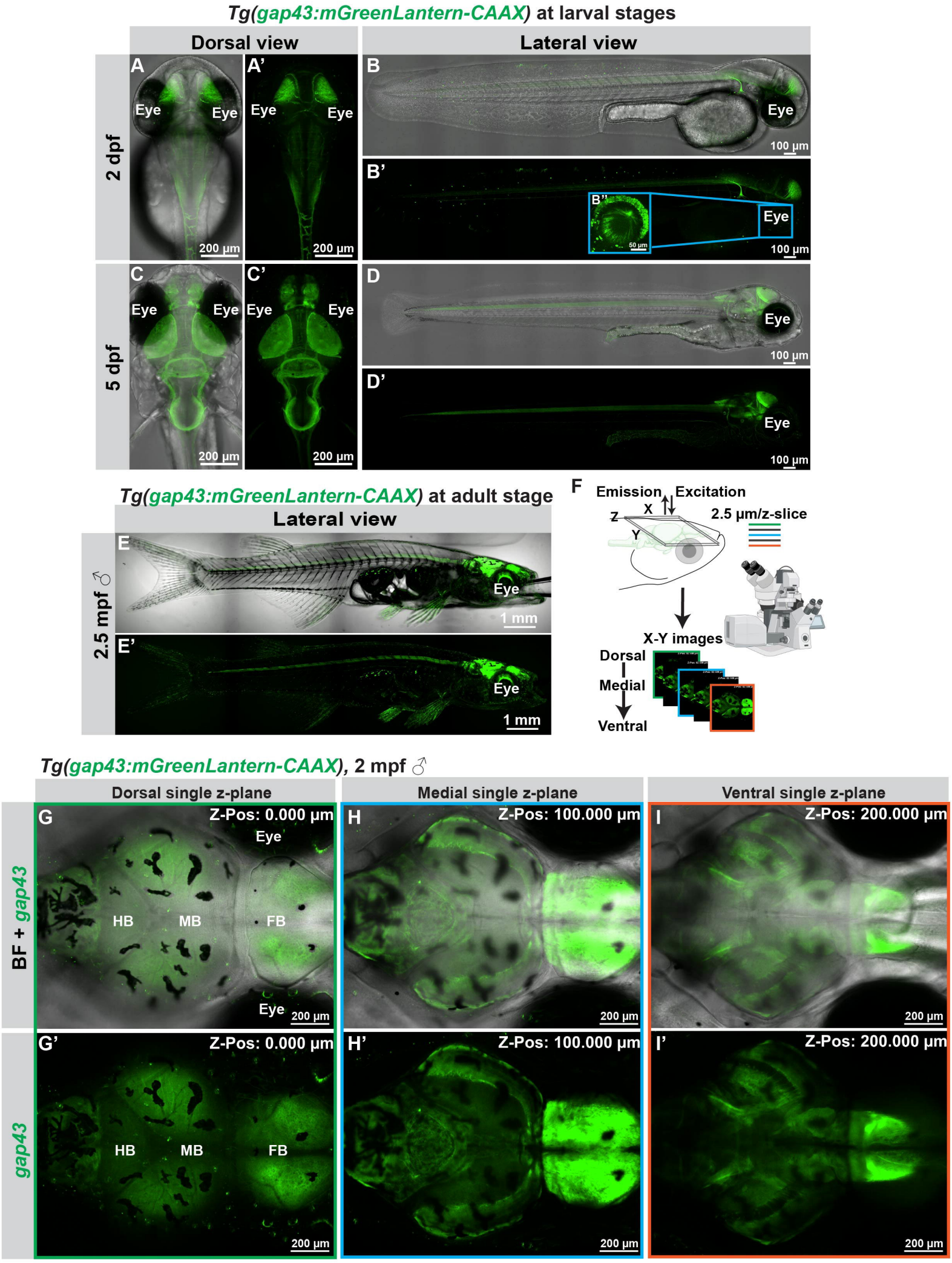
Tg(gap43:mGreenLantern-CAAX) at larval stages
Dorsal view
Lateral view
2 dpf
5 dpf
A
A'
B
B'
B''
C
C'
D
D'
Eye
200 µm
100 µm
50 µm
Tg(gap43:mGreenLantern-CAAX) at adult stage
Lateral view
2.5 mpf ♂
E
E'
1 mm
F
Emission
Excitation
X
Z
Y
2.5 µm/z-slice
X-Y images
Dorsal
Medial
Ventral
Tg(gap43:mGreenLantern-CAAX), 2 mpf ♂
Dorsal single z-plane
Medial single z-plane
Ventral single z-plane
BF + gap43
gap43
G
G'
H
H'
I
I'
Z-Pos: 0.000 µm
Z-Pos: 100.000 µm
Z-Pos: 200.000 µm
HB
MB
FB

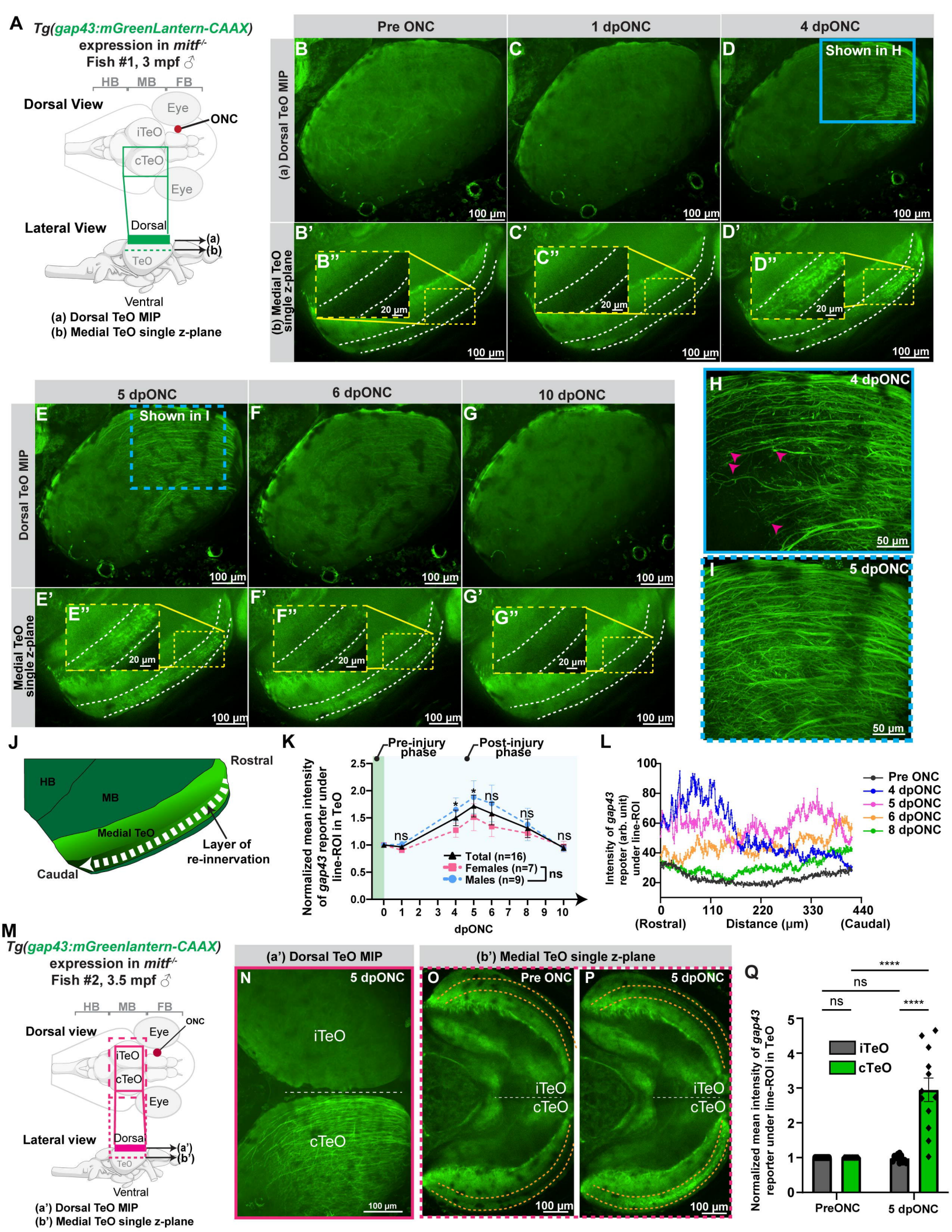
A
Tg(gap43:mGreenLantern-CAAX)
expression in mitf-/-
Fish #1, 3 mpf ♂
HB
MB
FB
Dorsal View
Eye
ONC
iTeO
cTeO
Eye
Lateral View
Dorsal
(a)
(b)
TeO
Ventral
(a) Dorsal TeO MIP
(b) Medial TeO single z-plane
Pre ONC
1 dpONC
4 dpONC
(a) Dorsal TeO MIP
(b) Medial TeO single z-plane
Shown in H
100 µm
20 µm
5 dpONC
6 dpONC
10 dpONC
Dorsal TeO MIP
Medial TeO single z-plane
Shown in I
50 µm
J
Rostral
HB
MB
Medial TeO
Layer of re-innervation
Caudal
K
Pre-injury phase
Post-injury phase
Normalized mean intensity of gap43 reporter under line-ROI in TeO
Total (n=16)
Females (n=7)
Males (n=9)
ns
dpONC
L
Intensity of gap43 repoter (arb. unit) under line-ROI
Pre ONC
4 dpONC
5 dpONC
6 dpONC
8 dpONC
(Rostral)
Distance (µm)
(Caudal)
M
Tg(gap43:mGreenlantern-CAAX)
expression in mitf-/-
Fish #2, 3.5 mpf ♂
Dorsal view
Lateral view
(a')
(b')
(a') Dorsal TeO MIP
(b') Medial TeO single z-plane
(a') Dorsal TeO MIP
(b') Medial TeO single z-plane
5 dpONC
Pre ONC
iTeO
cTeO
Q
Normalized mean intensity of gap43 reporter under line-ROI in TeO
PreONC
5 dpONC

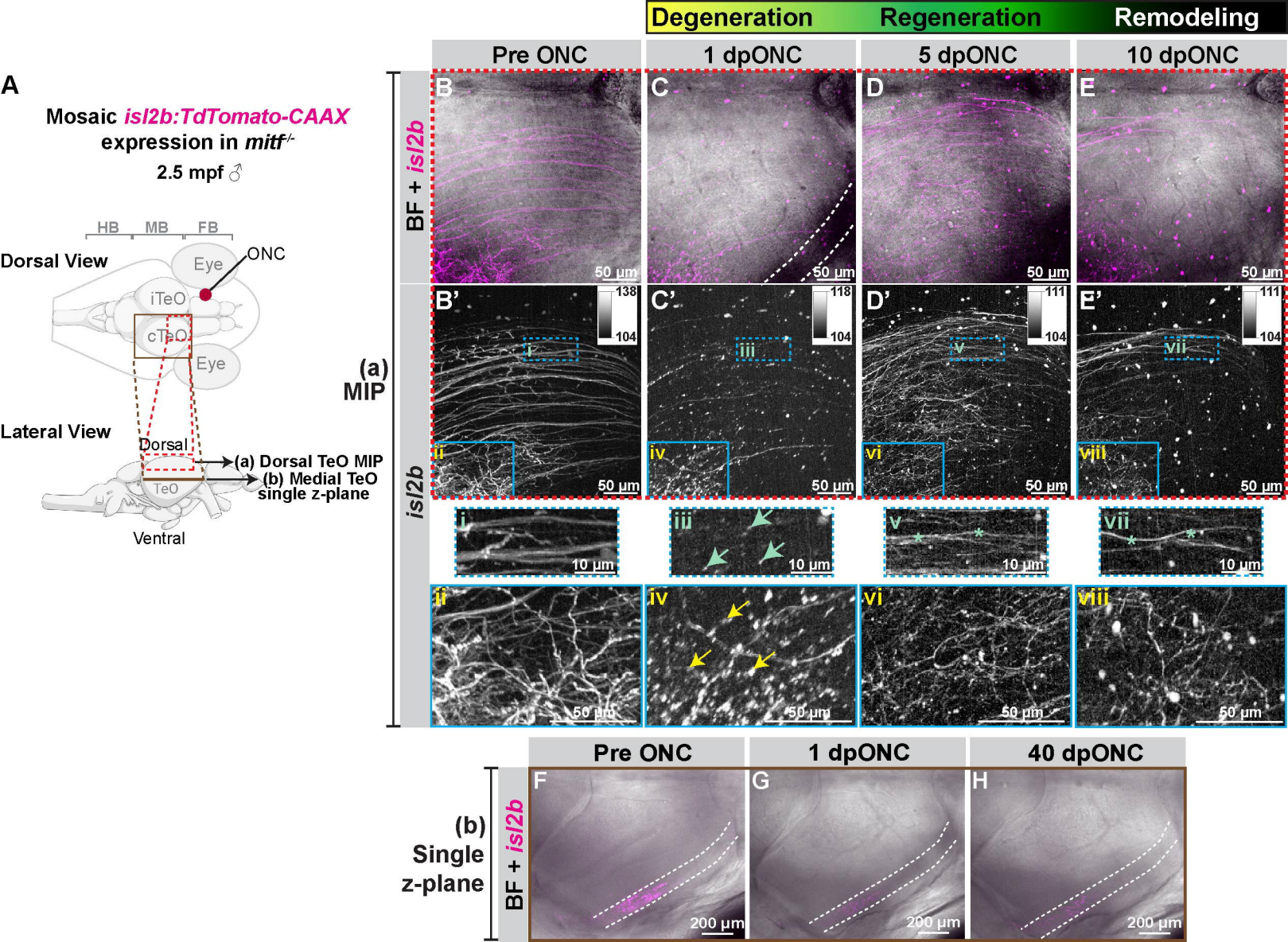
Degeneration
Regeneration
Remodeling
A
Mosaic isl2b:TdTomato-CAAX expression in mitf-/-
2.5 mpf ♂
HB
MB
FB
Dorsal View
Eye
ONC
iTeO
cTeO
Eye
Lateral View
Dorsal
(a) Dorsal TeO MIP
(b) Medial TeO single z-plane
TeO
Ventral
Pre ONC
1 dpONC
5 dpONC
10 dpONC
BF + isl2b
(a) MIP
isl2b
B
C
D
E
B'
C'
D'
E'
138
104
118
104
111
104
111
104
i
ii
iii
iv
v
vi
vii
viii
50 µm
10 µm
(b) Single z-plane
Pre ONC
1 dpONC
40 dpONC
F
G
H
200 µm

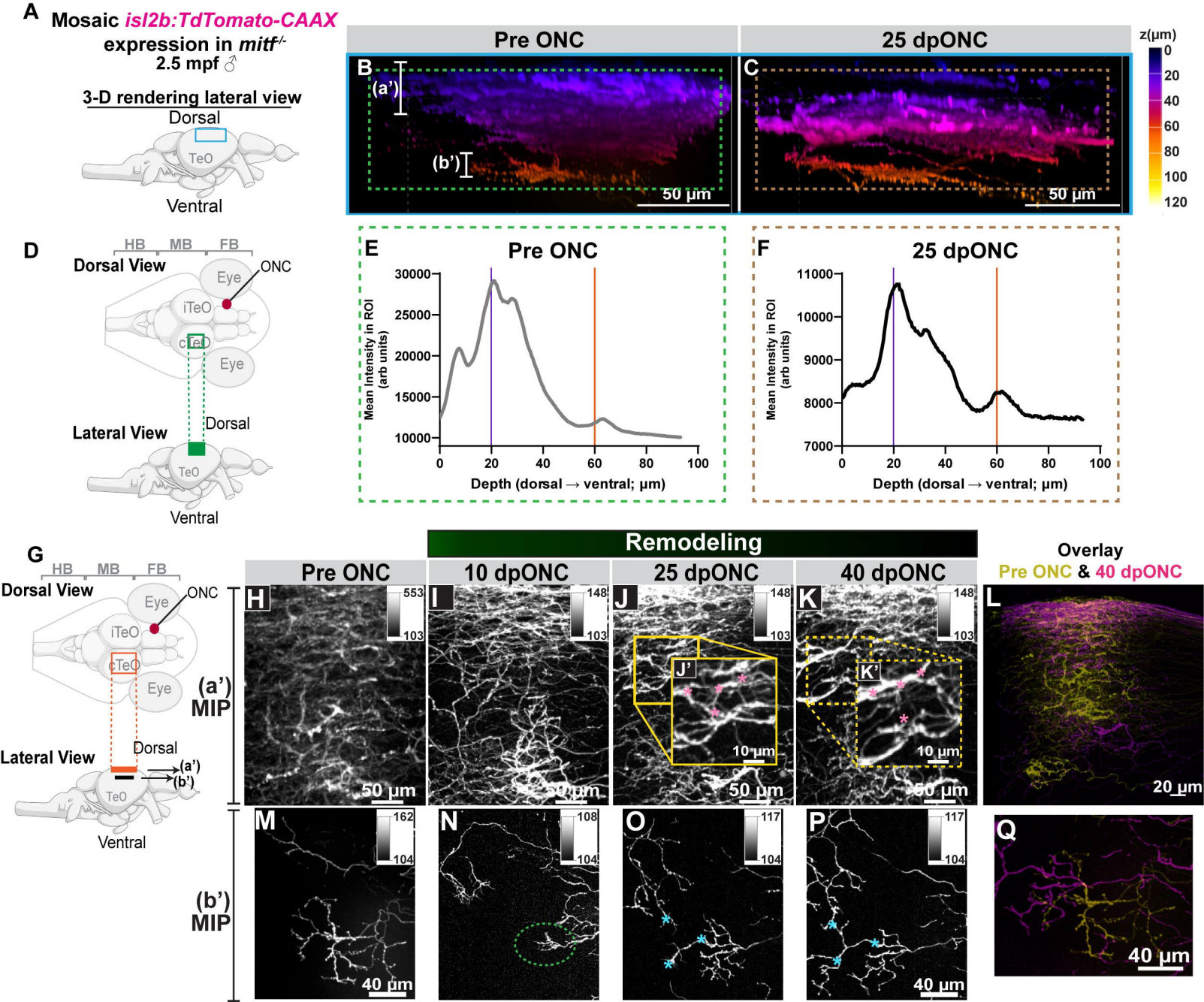
A
Mosaic isl2b:TdTomato-CAAX expression in mitf-/-
2.5 mpf ♂
3-D rendering lateral view
Dorsal
TeO
Ventral
Pre ONC
25 dpONC
z(µm)
0
20
40
60
80
100
120
B
(a')
(b')
50 µm
C
50 µm
D
HB
MB
FB
Dorsal View
ONC
Eye
iTeO
cTeO
Eye
Lateral View
Dorsal
TeO
Ventral
E
Pre ONC
Mean Intensity in ROI (arb units)
Depth (dorsal → ventral; µm)
F
25 dpONC
Mean Intensity in ROI (arb units)
Depth (dorsal → ventral; µm)
G
Remodeling
Pre ONC
10 dpONC
25 dpONC
40 dpONC
Overlay
Pre ONC & 40 dpONC
(a') MIP
(b') MIP
H
I
J
J'
K
K'
L
M
N
O
P
Q
50 µm
10 µm
20 µm
40 µm

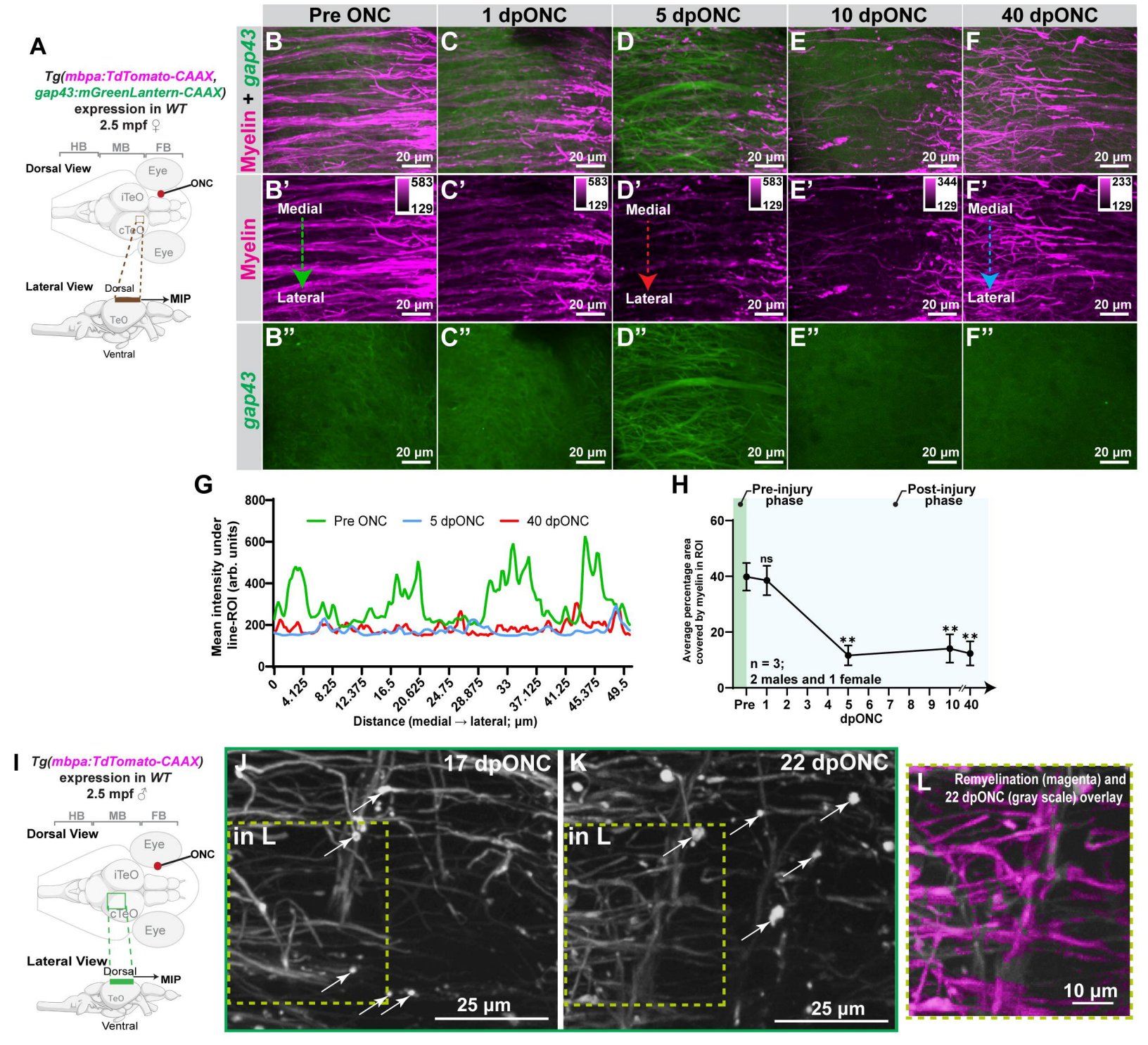
A
Tg(mbpa:TdTomato-CAAX, gap43:mGreenLantern-CAAX) expression in WT 2.5 mpf ♀
HB
MB
FB
Dorsal View
Eye
ONC
iTeO
cTeO
Eye
Lateral View
Dorsal
MIP
TeO
Ventral
Pre ONC
1 dpONC
5 dpONC
10 dpONC
40 dpONC
Myelin + gap43
Myelin
gap43
B
C
D
E
F
B'
C'
D'
E'
F'
B''
C''
D''
E''
F''
Medial
Lateral
583
129
344
233
20 µm
G
Mean intensity under line-ROI (arb. units)
Pre ONC
5 dpONC
40 dpONC
Distance (medial → lateral; µm)
H
Pre-injury phase
Post-injury phase
Average percentage area covered by myelin in ROI
ns
**
n = 3;
2 males and 1 female
dpONC
I
Tg(mbpa:TdTomato-CAAX) expression in WT 2.5 mpf ♂
J
17 dpONC
K
22 dpONC
in L
25 µm
L
Remyelination (magenta) and 22 dpONC (gray scale) overlay
10 µm